Flopping-mode electron dipole spin resonance in the strong-driving regime

Julian D. Teske,[1,*] Friederike Butt,[1] Pascal Cerfontaine,[1] Guido Burkard,[2] and Hendrik Bluhm[1]
[1]*JARA-FIT Institute for Quantum Information, Forschungszentrum Jülich GmbH and RWTH Aachen University, 52074 Aachen, Germany*
[2]*Department of Physics, University of Konstanz, 78457 Konstanz, Germany*

(Received 25 August 2022; revised 21 November 2022; accepted 20 December 2022; published 5 January 2023)

Achieving high-fidelity control of spin qubits with conventional electron dipole spin resonance (EDSR) requires large magnetic field gradients of about 1 mTnm^{-1}, which also couple the qubit to charge noise, and large drive amplitudes of order 1 mV. The flopping mode is an alternative method to drive EDSR of an electron in a double quantum dot, where the large displacement between both dots increases the driving efficiency. We propose to operate the flopping mode in the strong-driving regime to use the full magnetic field difference between the two dots. In simulations, the reduced required magnetic field gradients suppress the infidelity contribution of charge noise by more than two orders of magnitude, while providing Rabi frequencies of up to 60 MHz. However, the near degeneracy of the conduction band in silicon introduces a valley degree of freedom that can degrade the performance of the strong-driving mode. This necessitates a valley-dependent pulse optimization and makes operation to the strong-driving regime questionable.

DOI: 10.1103/PhysRevB.107.035302

I. INTRODUCTION

In recent years, semiconductor qubits have developed tremendously with key results being fidelities above the error correction threshold [1,2] and small-scale quantum processors [3,4] (see [5] for a recent review). New proposals to construct a universal quantum computer based on this qubit type have been formulated [6,7]. Supporting the long-term perspective, semiconductor qubits were shown to be compatible with classical complementary metal-oxide semiconductor (CMOS) technology [8,9] and can be operated at temperatures above 1 K [10,11]. Furthermore, there has been progress in the transport of single charges [12] and of spin qubits through semiconductor quantum dot arrays, with the objective of establishing medium-range coupling interaction [13,14], offering much higher connectivity than next-nearest-neighbor coupling.

A well-established technique for the manipulation of a single spin in a quantum dot (QD) is the electron dipole spin resonance (EDSR), where a spin-orbit coupling can be naturally present in the material [15] or artificially induced by an inhomogeneous magnetic field [16]. This spin-orbit coupling is used to drive spin transitions by resonantly shifting the position of the QD with an electric signal. Another method is the driving of electron spin resonance (ESR) with microwaves emitted by a nanoscale transmission line in proximity of the QDs. However, EDSR is often considered as the method of choice because it allows driving with purely electric fields, which are easier to localize and dissipate less energy than the AC currents needed for ESR. The energy dissipation is especially important when cryogenic electronics are involved in the pulse generation.

To identify possibilities to improve EDSR, a detailed assessment of its requirements and limitations is required. While fidelities of 99.95%, sufficient for quantum error correction, have been reached, the required strong magnetic field gradients couple the electron spin to electric noise, which was identified as the main limitation of the achievable fidelity [17,18]. In conclusion, a method requiring smaller field gradients would let the qubit tolerate larger electric noise, for example, due to a higher operating temperature or noisy, power-limited cryoelectronics.

Furthermore, the strong confinement on an electron in a QD necessitates relatively strong driving signals with a substantial power dissipation to reach typical Rabi frequencies in the MHz range [17]. Working at lower magnetic fields would be advantageous because the resulting lower drive frequencies can be expected to reduce crosstalk because lower frequencies reduce capacitive cross coupling and it would simplify the realization of ultra-low-power cryoelectronic control solutions. However, the total magnetic field $\vec{B}_0$ must be compatible with the required magnetic field gradient, as the local inhomogeneous magnetic fields $\vec{B}_{\mathrm{loc}}(\vec{x})$ are usually provided by micromagnets, which are magnetized by $\vec{B}_0$ [19]. Large field gradients require optimized magnet designs with special shapes, which increase the complexity of designing scalable layouts. Moreover, it is difficult to achieve a total magnetic field $\vec{B}(\vec{x}) = \vec{B}_{\mathrm{loc}}(\vec{x}) + \vec{B}_0$ much smaller than the micromagnet field, as the externally applied field $\vec{B}_0$ would then have to largely cancel out the micromagnet field. Foreseeable variation of the latter between qubits will hamper a strong cancellation for many qubits at a time.

One approach to working with lower magnetic field gradients is the flopping-mode driving scheme, which applies the EDSR principle to an electron confined in a double quantum dot (DQD). Instead of shifting the position of a single QD, the driving electric signal changes the potential difference

*julian.teske@rwth-aachen.de

of the two dots in the DQD, displacing the electron within the DQD. This displacement provides a large electric dipole moment, while being more efficient in terms of driving power than shifting a QD [20,21]. The distance of the two dots is usually on the order of 100 nm, whereas the displacement of the QD in conventional EDSR is typically only 1 nm. This increases the dipole moment and allows the use of much smaller magnetic field gradients and smaller total magnetic fields. Smaller Zeeman splittings are also beneficial for spin relaxation time, especially in the case of silicon, if the Zeeman splitting is smaller than the valley splitting [22].

The flopping-mode qubit first attracted attention because its strong electric dipole moment enables strong spin-photon coupling in cavities [23–27]. This spin-photon coupling can also be used to mediate two-qubit gates [28]. Alternatively, two-qubit gates for the flopping mode can be implemented by capacitive coupling [29] and the flopping-mode can even be applied to heavy-hole qubits in germanium [30].

While the weak-driving regime considered in previous studies is most efficient when aiming for the lowest possible drive amplitude [20], improving the fidelity favors large drive amplitudes, thus eventually leaving the weak-driving regime. We thus propose and analyze a strong-driving regime for the flopping-mode qubit with a pulse amplitude much larger than the tunnel coupling of the DQD such that the electron is entirely shifted from one dot to the other, exploiting the full magnetic field gradient across the DQD. The central idea of our proposal is to let the electron oscillate resonantly between the stable and noise-insensitive positions of strong confinement in the left and right QD while spending as little time in the transition between the dots.

The concept of moving the electron between the discrete positions in the left and the right QD can also be supported by the driving pulse. We study a smoothed rectangular driving pulse that provides the maximal time of strong confinement between adiabatic transitions. As the electron is strongly confined in one QD most of the time, small perturbation to the pulse have only a weak effect on the electrons position.

Parallel to our studies, the strongly confined configuration was considered for the robust storage for quantum information and the transition into the weak-driving flopping-mode regime for manipulation was investigated [31]. This idea switches the strong dipole moment on and off between storage and manipulation to improve the noise robustness during idle time, while our proposal intends to use the robustness of strong confinement to improve the robustness of the manipulation.

The strong-driving flopping-mode qubit suits proposals for sparse architectures for a semiconductor spin quantum processor [7], where DQDs are readily available without requiring additional sites and crosstalk is suppressed by the large distances between qubits. The low magnetic field is also beneficial in shuttling-based quantum processors [6]. Furthermore, the proposed pulse scheme poses only minimal requirements concerning the pulse generation electronics.

We simulate the flopping mode to calculate the achievable fidelity in presence of noise. We show the reduced noise sensitivity by the transition from the weak- to the strong-driving regime. In the strong-driving regime we discuss two different pulse shapes to fully leverage the potential of flopping mode. We identify optimal parameter regions where a good noise resilience is achieved while the probability for orbital excitation is minimized. Leakage by orbital excitation poses the limiting factor for the performance in the general model (without valley states). We calculate excellent fidelities with an improvement of more than two orders of magnitude in fidelity compared to conventional EDSR.

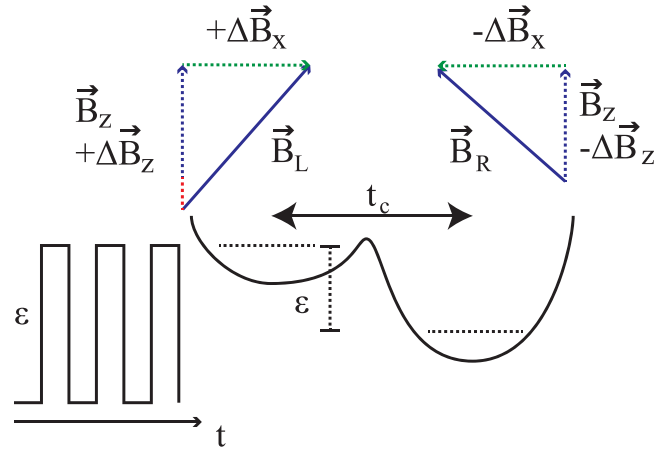

FIG. 1. Sketch of the flopping-mode qubit. An electron is trapped in a DQD of tunnel coupling t_c and the detuning ϵ corresponds to the energy difference of the ground state in the left and right QDs. The electron's wave function is shifted between the left and right QDs by an electric pulse on the detuning. Here, a rectangular pulse is drawn for the manipulation. The magnetic field gradient ΔB_x introduces an artificial spin-orbit coupling that allows Rabi driving of the spin state. The total magnetic field $\vec{B}_z$ determines the Zeeman energy and hence the resonance frequency of the qubit.

To discuss the realization of the strong-driving regime of the flopping mode in Si-based devices, we include different valley states in our model. The valley splitting has been argued to be a local stochastic material parameter [32] that is difficult to control. Valley excitations can degrade the performance of the flopping mode so that pulses have to be optimized specifically for a given valley splitting. In the strong-driving regime, high-fidelity manipulation can only be realized with a favorable valley splitting configuration so that high-fidelity operation may in general be constrained to the weak-driving regime.

The remainder of this paper is structured as follows. In Sec. II, we present our qubit model and two pulse schemes to drive the flopping-mode qubit. In Sec. III, we present the results of our simulation. In Sec. IV, we extend the simulation to discuss implications of the valley degree of freedom (DOF) for flopping-mode qubits in silicon and in Sec. V we give an outlook and summarize our results.

II. MODEL

We model the flopping-mode qubit as single electron in a DQD placed in an inhomogeneous magnetic field as sketched in Fig. 1. We label the QDs left (L) and right (R) and assume different magnetic field values in the QDs $\vec{B}_L$ and $\vec{B}_R$. The coordinate system is chosen such that the total magnetic field $\vec{B}_L + \vec{B}_R$ is aligned with the z axis and the perpendicular component $\Delta\vec{B}_x$ of magnetic field gradient is aligned with the

x axis. We publish an implementation of the qubit model and the pulse shapes in the QOPT applications repository [33].

A. Hamiltonian

The Hamiltonian of an electron in a DQD with the convention $\hbar = 1$ is given by [21]

$$H(\epsilon(t)) = \frac{\epsilon(t)}{2}\tau_z + t_c\tau_x + \frac{E_z}{2}\sigma_z + \frac{g\mu_B}{2}(\Delta B_x\sigma_x + \Delta B_z\sigma_z)\tau_z, \quad (1)$$

where the detuning ϵ is the difference in the electric potentials of the two dots as function of time t and the tunnel coupling t_c of the two dots is assumed constant. The Zeeman energy is denoted $E_z = g\mu_B B_z$ with the effective g-factor g, Bohr magneton μ_B, and the magnetic field gradient in x direction (z direction) ΔB_x (ΔB_z). The Pauli matrices on the spin and orbital DOF are denoted σ and τ, and operate on the basis $(|\uparrow\rangle, |\downarrow\rangle)$ and $(|L\rangle, |R\rangle)$, respectively. The orbital degree of freedom $(|L\rangle, |R\rangle)$ is not to be confused with different orbital states of an electron in a single dot and we do not make assumptions about the explicit shape of the electric potential forming the dots. In particular, shifts of the QDs (used for traditional EDSR) are not included. These shifts contribute to variations of the magnetic fields, but can be neglected because the magnetic field gradients are about 100 times smaller than those used for standard EDSR [17] in the regime of interest.

The energy spectrum of the Hamiltonian defined in Eq. (1) is plotted in Fig. 2. The assumption of a small Zeeman splitting compared to the tunnel coupling $E_z \ll t_c$ leads to a dominant orbital splitting and a large avoided crossing between eigenstates with different orbital states. Thus, with our manipulation method we want to drive spin excitations between the ground state and the first-excited state while being adiabatic with respect to the orbital DOF. This driving is mediated by ΔB_x while we assume a finite ΔB_z to account for a placement tolerance of the micromagnet. For concreteness, we assume a conservative ratio of $\Delta B_x/\Delta B_z = 5$, whereas even higher ratios have already been realized [20].

We include three noise contributions in our model and we use the term *quasistatic* for noise contributions at frequencies much slower than the qubit dynamics. First, we consider noise on the detuning $\epsilon \to \epsilon(t) + \delta\epsilon(t)$, where quasistatic noise $\delta\epsilon$ is sampled from a Gaussian distribution. The second contribution is described as fast white noise $\delta\epsilon(t)$ with a constant spectral noise density S up to a finite cutoff frequency. Third, we describe the hyperfine interaction as quasistatic magnetic noise on the Zeeman splitting $E_z \to E_z + g\mu_B\delta B_z$ with a standard deviation σ_B. The contribution of charge noise to the quasistatic magnetic noise is suppressed by the low magnetic field gradients.

B. Pulse shapes

We investigate two pulse shapes. The first one is a cosine pulse with an envelope and the second pulse is a smoothed rectangular function [Fig. 4(a)]. The cosine pulse is given by

$$\epsilon(t) = \epsilon_0 + 2\,\sin^2\left(\frac{\pi t}{T}\right)A\,\cos(\omega t + \phi), \quad (2)$$

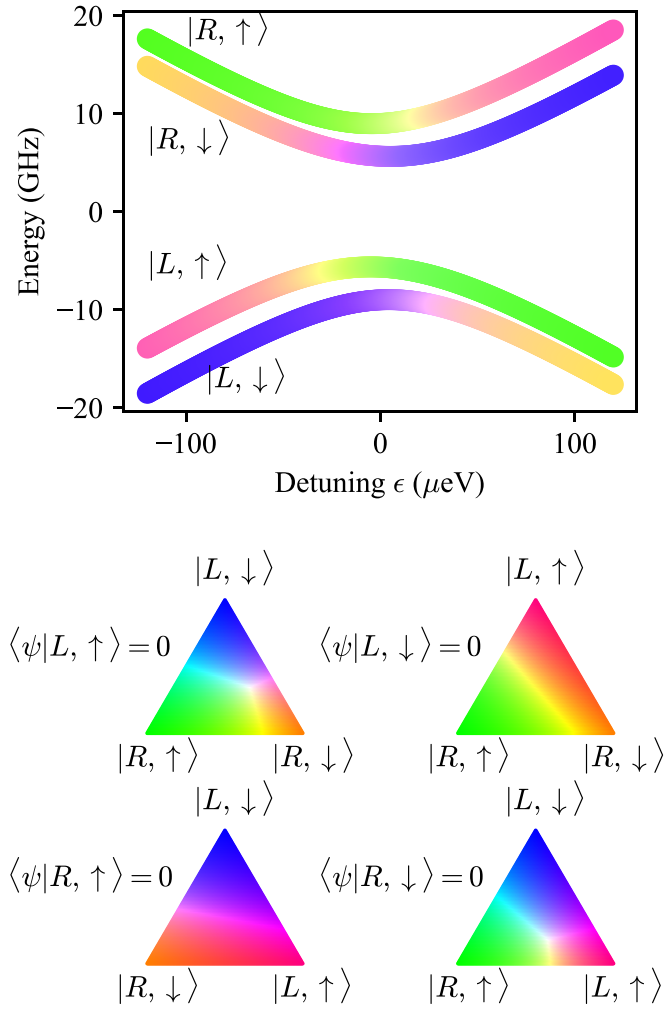

FIG. 2. Energy spectrum of the flopping-mode qubit. The energies of the eigenstates are plotted against the detuning of the DQD. The colors encode the changes in the eigenstates as visualized by the triangles below. Each triangle shows the color code for superpositions of three basis states. Each corner of the triangles corresponds to one basis state, each edge to superpositions of two basis states, and the interior of the triangle is filled with nonzero superpositions of all three eigenstates. The orbital states show an avoided crossing due to the tunnel coupling $t_c = 30\,\mu$eV. The energy of the spin states is split by the Zeeman energy $E_z/g\mu_B = 120\,$mT with the asymmetry introduced by the magnetic gradient along the z axis $\Delta B_z = 40\,$mT. The two lowest-lying energy states differ by their spin and transitions can be driven by the coupling magnetic gradient $\Delta B_x = 60\,$mT. The large magnetic field values were chosen to increase the clarity of the illustration.

with the offset ϵ_0, amplitude A, total pulse time T, carrier frequency ω, and phase offset ϕ. The $\sin^2$ term acts as an envelope and is scaled by the factor of 2 to have unity average amplitude.

The cosine pulse is not ideal concerning the three key properties heat dissipation, achievable Rabi frequency, and noise susceptibility. In terms of heat dissipation, in the strong-driving regime $A \gg 2t_c$, the occupation probability in one dot saturates such that the highest detuning peaks of the sine function do not contribute to the displacement of the

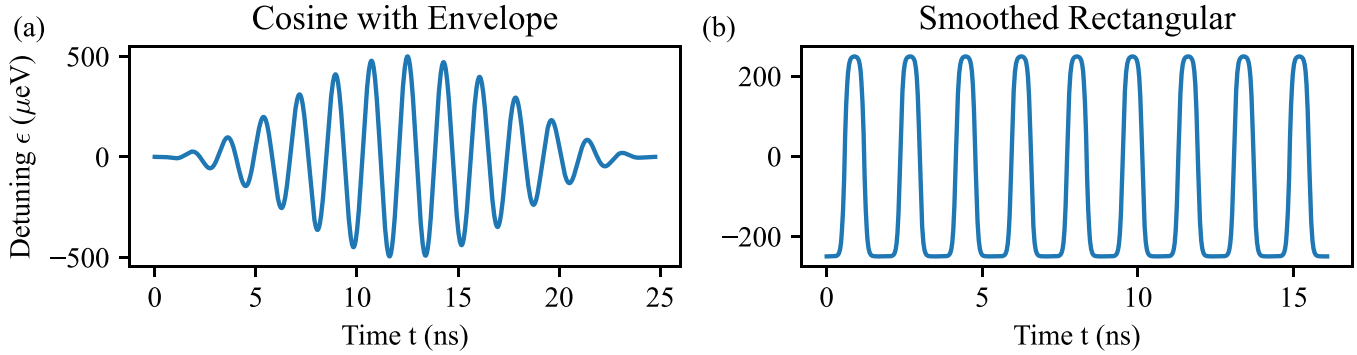

FIG. 3. Plots of the two considered pulse forms. (a) The cosine pulse with a sinusoidal envelope serves as reference pulse form. The pulse starts and ends in a symmetrically tuned DQD. (b) The smoothed rectangular pulse with a steepness parameter of $R_{\tanh} = 13$ represents the proposed pulse form. The asymmetry between positive and negative values is set by the duty cycle parameter $c_{\mathrm{dc}} = 0.3$. The rectangular pulse starts and ends in a strongly detuned DQD such that the electron is confined in one QD. Both pulses were plotted for illustration with $A = 250\,\mu\mathrm{eV}$, $T_{\mathrm{res}} = 2\pi/\omega \approx 0.56\,\mathrm{ns}$, and $T \approx 25\,\mathrm{ns}$ and $T \approx 16\,\mathrm{ns}$ for the cosine and rectangular pulse, respectively.

electron, while they still contribute to the heat emission of the high-frequency signal. The achievable Rabi frequency is limited because the electron is not fully displaced during the initial and final oscillations of the pulse due to the envelope. And finally the noise susceptibility is not ideal yet because the electron's wave function is stretched over the DQD for a large portion of the pulse yielding a high spin-orbit mixing on average.

We envision the ideal pulse to meet the following three requirements to improve with respect to the three key properties. First, the pulse starts and terminates localized in one QD. Second, the electron is strongly localized in one QD during as much of the pulse duration as possible without the amplitude reaching unnecessarily high values. Third, the electron is shifted between the two dots as fast as possible to reduce noise susceptibility, while still being transferred adiabatically with regard to both charge and spin excitations.

We implement such a pulse with a smoothed rectangular pulse shape [Fig. 3(b)]. The rectangular pulse is modeled in the simulation by transitions shaped as hyperbolic tangent functions:

$$\begin{aligned}
&\epsilon(t) = A\,\tanh\left[\frac{2R_{\tanh}}{T_{\mathrm{res}}}\left(t - \frac{T_{\mathrm{res}}(1+c_{\mathrm{dc}})}{4}\right)\right],\\
&\forall\, t : t = nT_{\mathrm{res}} + s,\, s < T_{\mathrm{res}}/2,\, n \in \mathbb{N},\\
&\epsilon(t) = -A\,\tanh\left[\frac{2R_{\tanh}}{T_{\mathrm{res}}}\left(t - \frac{T_{\mathrm{res}}(3-c_{\mathrm{dc}})}{4}\right)\right],\\
&\forall\, t : t = nT_{\mathrm{res}} + s,\, s > T_{\mathrm{res}}/2,\, n \in \mathbb{N},
\end{aligned} \tag{3}$$

where $T_{\mathrm{res}} = \frac{2\pi}{E_z}$ is the resonance oscillation period, $R_{\tanh}$ the pulse steepness, and the duty cycle parameter $c_{\mathrm{dc}} \in [0, 1]$ effectively controls the Rabi frequency. This control is required because the amplitude cannot be used for the control of the Rabi frequency in the strong-driving regime due to saturation effects. The duty cycle parameter introduces an asymmetry such that the electron remains longer in one QD than in the other as can be seen in Fig. 3(b). Intuitively, c_{dc} determines the time the spin is exposed to the driving field. For $c_{\mathrm{dc}} = 0$ the driving is symmetric between both QDs providing the largest Rabi frequency possible and for $c_{\mathrm{dc}} = 1$ the electron remains stationary in one QD. Negative values for c_{dc} are possible but have the same effect with exchanged QDs and are not used in our formulation. The pulse steepness $R_{\tanh}$ is introduced to control the velocity of the charge transfer within the DQD, where a large $R_{\tanh}$ corresponds to a sharper rectangle and therefore a faster charge transfer.

We require the total pulse time to be an integer multiple of the resonance period time, such that the electron is always driven in full cycles and terminates in the same QD as it started. This complicates the pulse tuning as it makes the time a discrete optimization parameter. We use the duty cycle parameter to adjust the effective driving strength to the pulse time. Note that two single-qubit gates about orthogonal axes can be acquired by a phase shift of the pulse by $\pm\pi/4$.

C. Methods

We performed quantum dynamics simulations of the proposed pulses using the simulation and optimal control package QOPT [34]. Before the optimal performance of the flopping-mode qubit can be evaluated, the pulses must be optimized for a given magnetic field and DQD parameters because the inaccuracy of analytic estimates of the optimal pulse parameters would deteriorate the qubit performance. The numeric optimization allows us to estimate the optimal pulse length and frequency (T, ω) for the cosine pulse or the optimal pulse length and duty cycle parameter (T, c_{dc}) for the rectangular pulse with great accuracy.

A suitable figure of merit for the quantification of the qubit performance needs to account for the spin dynamics and excitations in the orbital DOF, which we consider to be leakage. Therefore, we define an infidelity $\mathcal{I}_L$ in the presence of leakage between the calculated propagator U and a target unitary U_{target} as

$$\mathcal{I}_L(U_{\mathrm{target}}, U) = 1 - \tfrac{1}{4}|\mathrm{tr}(U_{\mathrm{target}}^{\dagger} U|_{V_C})|^2, \tag{4}$$

where $U|_{V_C}$ denotes the truncation of the propagator to the computational subspace. The measure $\mathcal{I}_L$ always considers leakage as erroneous and thus $\mathcal{I}_L > 0$ for a finite probability of orbital excitation during the pulse. For example, if we take the target to be identity $U_{\mathrm{target}} = I$ and the propagator to include orbital excitation $U(x) = \exp(xi\pi\tau_x/2)$, then we calculate $\mathcal{I}_L(I, U(x)) = 1 - [\cos(x\pi) + 1]/2$. The definition is

inspired by common fidelity measures [35]. Our optimization target U_{target} is an X_π gate in the computational space, but the pulse-optimization algorithm can be adapted to any rotation around the x axis. Other fidelity measures can also be used to assess the performance in specific situations. For example, if the fidelity of an experiment shall be predicted, then the simulation can be extended by an orbit-independent spin measurement, implemented as partial trace over the orbital DOF. The average gate fidelity for such a quantum channel can be calculated following [35,36]. Although the exact fidelities are deviating, we found the systematic relations and the interpretation to be independent of the fidelity measure.

We define the computational space in terms of the eigenvectors v_i, $1 \leqslant i \leqslant 4$, of the Hamiltonian at $t = 0$. We want to drive excitations in the spin DOF, so we define the computational space V_C to be the vector space that is spanned by the ground and the first-excited state with a different spin. With the assumption that $E_z < 2t_c$, we have

$$V_C = \text{span}(v_1, v_2). \tag{5}$$

If the orbital splitting $\Omega = \sqrt{\epsilon^2 + 4t_c^2}$ set by the tunnel coupling and offset in detuning becomes smaller than the Zeeman splitting, we need to replace v_2 with v_3. The leakage space is then defined to be spanned by the remaining eigenvectors. These definitions are justified by the assumption that the flopping-mode qubit is initialized and read out adiabatically. For the initialization, this means that the qubit is initialized as a Loss-DiVincenzo qubit and then adiabatically transferred into the DQD with detuning $\epsilon(t = 0)$. To perform the readout, the electron is first adiabatically confined in one QD and then read out as Loss-DiVinvenzo qubit.

To study the noise resilience of the proposed driving mode, we perform Monte Carlo noise simulations of quasistatic and white noise. For the simulation of quasistatic noise, we average over eight noise values $\delta\epsilon$ to approximate an integral over a Gaussian distribution. For white noise we generate 1000 time-dependent noise traces $\delta\epsilon(t)$ from the spectral noise density with pseudorandom numbers. The effect of quasistatic noise is calculated in a basis adiabatically following the noise, meaning that the eigenvectors defining the computational space are calculated for the Hamiltonian $H(\epsilon(t = 0) + \delta\epsilon)$.

The tuning procedure is described in more detail in the Supplemental Material in Appendix A. We verified the simulation by reproducing previous experimental and theoretical results as discussed in Appendixes D and E.

III. RESULTS

In this section, we consider sources of strong quasistatic electric noise with a standard deviation of $\sigma_\epsilon = 15\,\mu\text{eV}$ and white noise with a spectral noise density of $S = 0.07\,\mu\text{eV}/\sqrt{\text{Hz}}$ and a cutoff at 10 GHz. We chose noise values larger than those typically measured in experiments [17,37] to demonstrate the noise resilience of the proposed driving mode. We choose to evaluate the flopping-mode qubit in a small magnetic field $E_z/(g\mu_B) = 20\,\text{mT}$ with a transversal magnetic field gradient $\Delta B_x = 2\,\text{mT}$ and a longitudinal gradient $\Delta B_z = 0.4\,\text{mT}$, unless stated otherwise.

We also consider quasistatic fluctuations of the Zeeman splitting E_z with a standard deviation of $\sigma_B = 3\,\mu\text{T}$. Such a magnetic noise can for example originate from fluctuations of nuclear spins that couple to the electron spin in the DQD. Our value for σ_B is chosen lower than measured values in natural silicon [38] but higher than measurements in isotopically purified silicon suggest [18]. The value we chose corresponds to a residual ^{29}Si concentration of 0.5% or a dephasing time of $T_2^* = \hbar/\sigma_B \approx 1.9\,\mu\text{s}$ [39]. Even for the relatively high σ_B, perturbations from hyperfine noise can be neglected as they are dominated by the electrical noise and lead to an additional infidelity of about 10^{-5}, depending mainly on the pulse time T. We verified the consistency of our simulations with previous theoretical (see Appendix E) and experimental results (see Appendix D).

A. Pulse shape comparison

A direct comparison of the cosine and the rectangular pulse is made in Fig. 4. Figures 4(a) and 4(b) show the performance of the cosine pulse in the presence of electric noise. In Fig. 4(a), a clear improvement in the fidelity with larger amplitude can be observed except for very large amplitude values paired with a small tunnel coupling. In this case the infidelity is dominated by leakage into the excited orbital state caused by diabatic Landau-Zener (LZ) excitation. The green dotted lines are contour lines of the Rabi frequency showing the acceleration of the pulse with rising amplitude. The blue lines are contour lines of the infidelity. Note that the contour lines for the infidelity and the Rabi frequency are not parallel. This indicates that the increase in fidelity is not determined by the relation of the dephasing time to the pulse time T alone. Instead, it originates partially from the stronger confinement in one of the dots by larger absolute pulse values since the system is less susceptible to noise when the detuning ϵ is large and the spin-orbit mixing low.

Figures 4(c) and 4(d) show corresponding plots for the rectangular pulse, where t_c is kept constant, because $t_c = 100\,\mu\text{eV}$ is the global optimum (compare Fig. 5) and R_{tanh} is varied to map out the strong-driving regime. The steplike features in the Fig. 4(c) are caused by the discreteness in the tuning of the rectangular pulse. The rectangular pulse time T must always be a multiple of the resonance time $T = n\frac{2\pi}{E_z}; n \in \mathbb{N}$. At every change of T, the Rabi frequency is increased and also the duty cycle parameter c_{dc} has a discontinuity. On each step, the infidelity drops and then continuously increases with the amplitude. This behavior is linked to c_{dc} because large duty cycle values correspond to asymmetric pulses, which are more susceptible to electric noise. The largest infidelity values in Figs. 4(c) and 4(d) arise for very steep pulses at large amplitudes and this infidelity contribution is caused by LZ excitation. The peaks in Fig. 4(d) [more clearly visible in Fig. 5(d)] near the green lines reflect coherent errors that are caused by pulse tuning. At these values, the total pulse time is shorter than ideal and the duty cycle can only decrease the Rabi frequency. The optimum for the fidelity is reached at a discontinuity, which is a pathological case, because the exact position of the discontinuity and the values in its proximity depend on the choice of the pulse length. Changes to the optimization algorithm can vary the results at these points (compare Appendix A). However, this is not a serious limitation to the driving mode because the fidelity only degrades

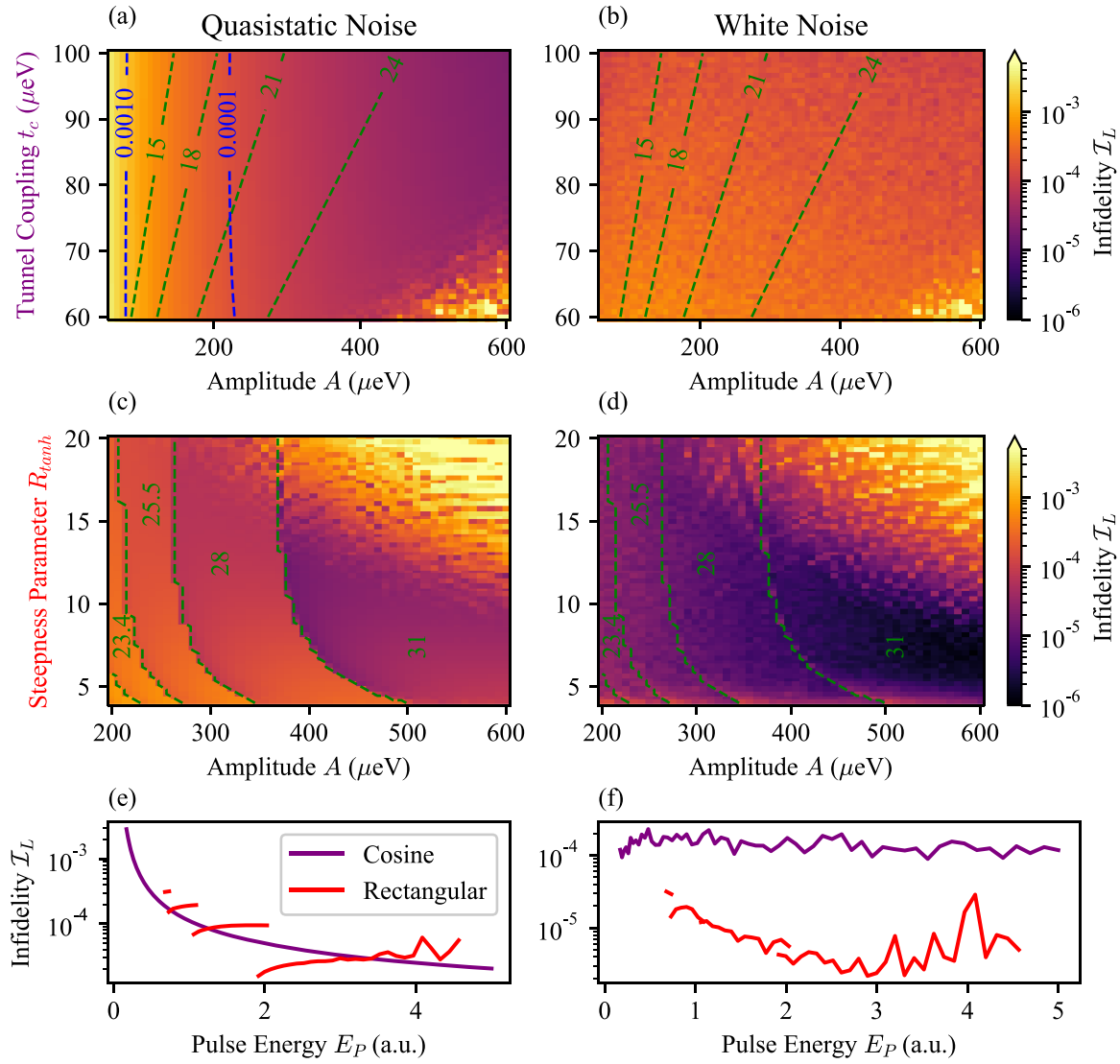

FIG. 4. Infidelity of the X_π gate calculated with Monte Carlo simulations of a flopping-mode qubit driven by a cosine pulse (a), (b) or a smoothed rectangular pulse (c), (d). The simulations include quasistatic noise on the control signal with a standard deviation of $\sigma_\epsilon = 15\,\mu\text{eV}$ in (a), (c), (e) and white noise with a spectral noise density of $\sqrt{S} = 0.07\,\text{neV}/\sqrt{\text{Hz}}$ in (b), (d), (f). Both simulations are performed with magnetic fields of $E_z/(g\mu_B) = 20\,\text{mT}$, $\Delta B_x = 2\,\text{mT}$, $\Delta B_z = 0.4\,\text{mT}$. The simulation of the rectangular pulse features a large tunnel coupling of $t_c = 100\,\mu\text{eV}$. The green dotted lines in (a) and (c) mark the contour lines of the Rabi frequency with values in MHz. (a) Contour lines of the fidelity are plotted in blue. The infidelity introduced by quasistatic noise is reduced for higher amplitudes unless LZ excitations increase the leakage for large amplitudes and small tunnel couplings. (b) The infidelity contribution by white noise is largely independent of the amplitude and tunnel coupling, unless LZ excitations are dominant. (c) We can identify an optimal region around $A = 400\,\mu\text{eV}$ and $R_{\text{tanh}} = 12$. For small amplitudes the pulse becomes slower and more susceptible to quasistatic noise while LZ excitations are dominant for steep pulses with a large amplitude. The Rabi frequency changes substantially at the discontinuities of the fidelity and is otherwise almost constant. The green Rabi frequency values correspond to the plateaus. (d) The rectangular pulse is robust towards white noise in a wide range of parameters. The plots in (e) and (f) show cuts along (a) and (c) and (b) and (d), respectively. The data are cut along $t_c = 100\,\mu\text{eV}$ and $R_{\text{tanh}} = 9.97$ to consider data of the same tunnel coupling and the optimal steepness R_{tanh}. Instead of the amplitude A, we plot the infidelity against the corresponding power dissipation $E_P(A)$. The rectangular pulse can achieve a higher fidelity and larger Rabi frequency with less power dissipation.

of about a factor of 2 when choosing pulse parameters away from the discontinuity.

Even though both pulses can reach robust noise insensitivity, the rectangular pulse has an advantage in terms of power dissipation. To quantify the pulse energy we define

$$E_P \propto \int [\epsilon(t) - \epsilon_0]^2 dt, \tag{6}$$

and plot in Figs. 4(e) and 4(f) the infidelity $\mathcal{I}_L$ against E_P for horizontal cuts through Figs. 4(a)–4(d). Figure 4(e) shows that a smaller infidelity can be reached with the rectangular pulse with a given E_P, if an optimal duty cycle can be chosen. From a comparison of the contour lines in Figs. 4(a) and 4(c) we can also extract that the rectangular pulse provides higher Rabi frequencies. The comparison of Figs. 4(b) and 4(d) also demonstrates that the

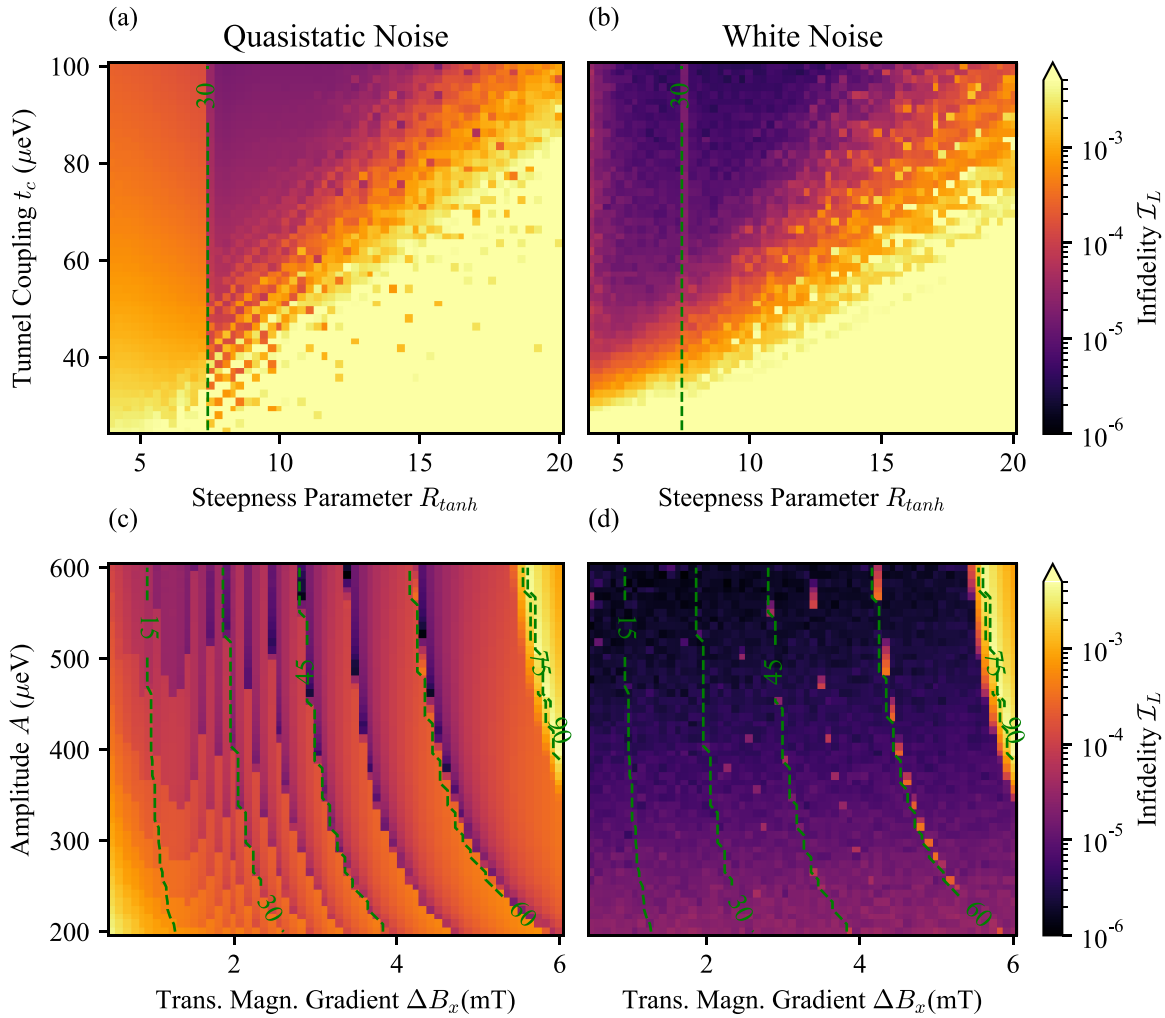

FIG. 5. Infidelity of the X_π gate calculated with Monte Carlo simulations of a flopping-mode qubit driven by a cosine pulse (a), (b) or a smoothed rectangular pulse (c), (d). The simulations include quasistatic noise on the control signal with a standard deviation of $\sigma_\epsilon = 15\,\mu$eV in (a), (c), (e) and white noise with a spectral noise density of $\sqrt{S} = 0.07\,\text{neV}/\sqrt{\text{Hz}}$ in (b), (d), (f). Both simulations are performed with magnetic fields of $E_z/(g\mu_B) = 20\,$mT, $\Delta B_x = 2\,$mT, $\Delta B_z = 0.4\,$mT. The simulation of the rectangular pulse features a large tunnel coupling of $t_c = 100\,\mu$eV. The green dotted lines in (a) and (c) mark the contour lines of the Rabi frequency with values in MHz. (a) Contour lines of the fidelity are plotted in blue. The infidelity introduced by quasistatic noise is reduced for higher amplitudes unless LZ excitations increase the leakage for large amplitudes and small tunnel couplings. (b) The infidelity contribution by white noise is largely independent of the amplitude and tunnel coupling, unless LZ excitations are dominant. (c) We can identify an optimal region around $A = 400\,\mu$eV and $R_{\text{tanh}} = 12$. For small amplitudes the pulse becomes slower and more susceptible to quasistatic noise while LZ excitations are dominant for steep pulses with a large amplitude. The Rabi frequency changes substantially at the discontinuities of the fidelity and is otherwise almost constant. The green Rabi frequency values correspond to the plateaus. (d) The rectangular pulse is robust towards white noise in a wide range of parameters. The plots in (e) and (f) show cuts along (a) and (c) and (b) and (d), respectively. The data are cut along $t_c = 100\,\mu$eV and $R_{\text{tanh}} = 9.97$ to consider data of the same tunnel coupling and the optimal steepness R_{tanh}. Instead of the amplitude A, we plot the infidelity against the corresponding power dissipation $E_P(A)$. The rectangular pulse can achieve a higher fidelity and larger Rabi frequency with less power dissipation.

rectangular pulse is less sensitive towards white noise in a wide region.

B. Landau-Zener excitation

Having identified leakage as one of the major sources of infidelity, we investigate the influence of leakage more closely. The shift of the electron from one dot to another can be theoretically described as a LZ transition. LZ theory predicts an excitation probability of $P_{\text{LZ}} = \exp(-2\pi\delta)$ with $\delta = t_c^2/4v$ with the level velocity $v = \frac{d\epsilon}{dt}$ [40]. A tight upper bound for the velocity of the rectangular pulse described in (3) can be calculated with a first-order Taylor expansion of the hyperbolic tangent to

$$v \leqslant \frac{2AR_{\text{tanh}}}{T_{\text{res}}} = \frac{AE_zR_{\text{tanh}}}{\pi}. \tag{7}$$

Thus, operation with low E_z is beneficial for the suppression of LZ excitation in addition to the advantages discussed above. In case of the amplitude A, a tradeoff must be made be since lower amplitudes further suppress LZ excitation and reduce the dissipated energy but also increase the noise sensi-

tivity. The plot in Figs. 5(a) and 5(b) explores the range of possible values for t_c and R_{tanh}, while keeping the relation $A = 4t_c$ to remain in the strong-driving regime. We observe that a higher tunnel coupling is generally favorable, while there is a sweet spot for R_{tanh} between an increase in LZ excitation and an increased noise sensitivity. In the absence of noise, we can clearly observe Landau-Zener-Stückelberg oscillations as discussed in the Appendix B.

The discreteness of the rectangular pulse can also be observed in Fig. 5. Like in Figs. 4(c) and 4(d), discontinuities in the sensitivity to quasistatic noise appear when the pulse time T changes. We do not observe an asymmetry around the steps for the infidelity caused by white noise. In Figs. 5(b) and 5(d) there are only tuning artifacts along the changes in the Rabi frequency, where the total pulse time is not optimal.

C. High Rabi frequencies

The achievable Rabi frequency is mainly determined by the transversal magnetic field gradient ΔB_x, while the influence of A saturates for large A values. The infidelity as function of ΔB_x and A is plotted in Figs. 5(c) and 4(d). The Rabi frequency ω_R can be brought up to values of more than 60 MHz, indicating that the rotating wave approximation $\frac{E_z}{\omega_R} \gg 1$ does not need to be fulfilled. The increased Rabi frequency reduces the influence of magnetic noise and for the assumed standard deviation of $\sigma_B = 3\,\mu\text{T}$ the infidelity contribution drops to 10^{-6}.

D. Comparison to conventional EDSR

The noise robustness of the flopping-mode qubit becomes evident in the direct comparison with EDSR in a single QD. In this section, we estimate the infidelity that arises, when a single QD is driven by EDSR and exposed to a charge noise source of the strength considered as the quasistatic electric noise above. We start with the rotating frame Hamiltonian for an electron in a QD under resonant drive, given by

$$H = \frac{\delta\omega}{2}\sigma_z + \frac{\omega_R}{2}\sigma_x, \tag{8}$$

where $\delta\omega$ denotes the frequency detuning of the driving signal from the resonance frequency and ω_R denotes the Rabi frequency. High fidelities were achieved by driving the electron with an electric control signal in a local magnetic field gradient with a transversal b_{trans} and a longitudinal b_{long} gradient. The transversal gradient determines the Rabi frequency $\omega_R = A_r g \mu_B b_{\text{trans}}/2$ with the amplitude of the displacement A_r.

The predominant contribution to the frequency detuning $\delta\omega$ originates from charge noise, which displaces the QD by a distance of δr and couples to the longitudinal magnetic field gradient $\delta\omega = \delta r g \mu_B b_{\text{long}}$ [17]. Both the driving pulse and the noise fluctuations shift the position of the QD over a distance of δr by creating a local electric field of strength δE. When approximating a QD as an harmonic confining potential with an orbital energy of Δ_{orb}, then the relation between positional shifts and applied electric fields is given by

$$\delta r = \frac{\hbar^2 e}{m_{\text{Si}}\Delta_{\text{orb}}}\delta E, \tag{9}$$

where m_{Si} denotes the effective electron mass in silicon and e the elementary charge (see Supplemental Material of [17]). Further, the electric field can be described by a shift in the electric potential δV:

$$\delta E = \frac{\delta V}{ed}, \tag{10}$$

where the distance d is measured from the QD to the charge defect creating δE. Let us assume that any defects causing charge noise and the driving metallic gates have the same distance to the QD of approximately $d \approx 100\,\text{nm}$.

The infidelity caused as pure dephasing by quasistatic noise for an X_π gate up to leading order is given by

$$\mathcal{I} \approx \left(\frac{\langle\delta\omega\rangle}{\omega_R}\right)^2 = \left(\frac{2\langle\delta V\rangle}{A}\frac{b_{\text{long}}}{b_{\text{trans}}}\right)^2. \tag{11}$$

A previous experiment achieved an optimal fidelity at a Rabi frequency of $\omega_R = 3.9\,\text{MHz}$, corresponding to a driving amplitude of $A = 70\,\mu\text{eV}$ for the magnetic field gradients $b_{\text{trans}} = 1\,\text{mTnm}^{-1}$ and $b_{\text{long}} = 0.2\,\text{mTnm}^{-1}$ [17]. We can now extrapolate the performance of this experiment for our assumption of quasistatic electric noise with a standard deviation of $\langle\delta V\rangle = 15\,\mu\text{eV}$ to an infidelity of $\mathcal{I} = 0.7\%$, which is more than two orders of magnitude larger compared to the optimal values in the flopping mode, where an infidelity of about $\mathcal{I}_L \approx 10^{-5}$ is predicted. In conclusion, the direct comparison to EDSR in a single QD for our assumed noise values demonstrates the much lower noise sensitivity of the flopping mode.

IV. FLOPPING-MODE EDSR IN SILICON

In this section, we discuss the prospects of realizing flopping-mode qubits in silicon, as it is the currently predominant material for the construction of spin qubit quantum processors [3,4]. The most relevant peculiarity of silicon is the conduction band degeneracy leading to the presence of a valley DOF. Silicon heterostructures possess two low-lying valley states that can influence the spin dynamics. Usually, the influence is modeled by a valley-dependent g-factor or a valley-orbit coupling mechanism.

The electron band structure of a two-dimensional electron gas in silicon has a twofold-degenerate minimum [41]. In the heterostructures used for the fabrication of semiconductor spin qubits, this degeneracy is lifted by the sharp potential step at a silicon-insulator interface [42,43]. The energy difference between these two valley states is called the valley splitting. We extend the Hamiltonian of (1) by the valley DOF

$$H_V = H + \sum_{i=L,R} P_i \begin{pmatrix} 0 & \Delta_i \\ \Delta_i^* & 0 \end{pmatrix}, \tag{12}$$

where P_L (P_R) denotes the projector on the left (right) QD, the valley splittings Δ_L and Δ_R are complex numbers, and the matrix is written in the valley basis ($|z\rangle$, $|\bar{z}\rangle$) consisting of two orthogonal valley states. Without loss of generality, we choose the quantization axis in the valley space such that the valley splitting in the left dot is purely real, i.e., $\text{Im}(\Delta_L) = 0$. The valley state influences the g-factor in silicon so that stochastic excitations lead to an increase in decoherence. We do not include a valley dependence of the g-factor, but we do consider

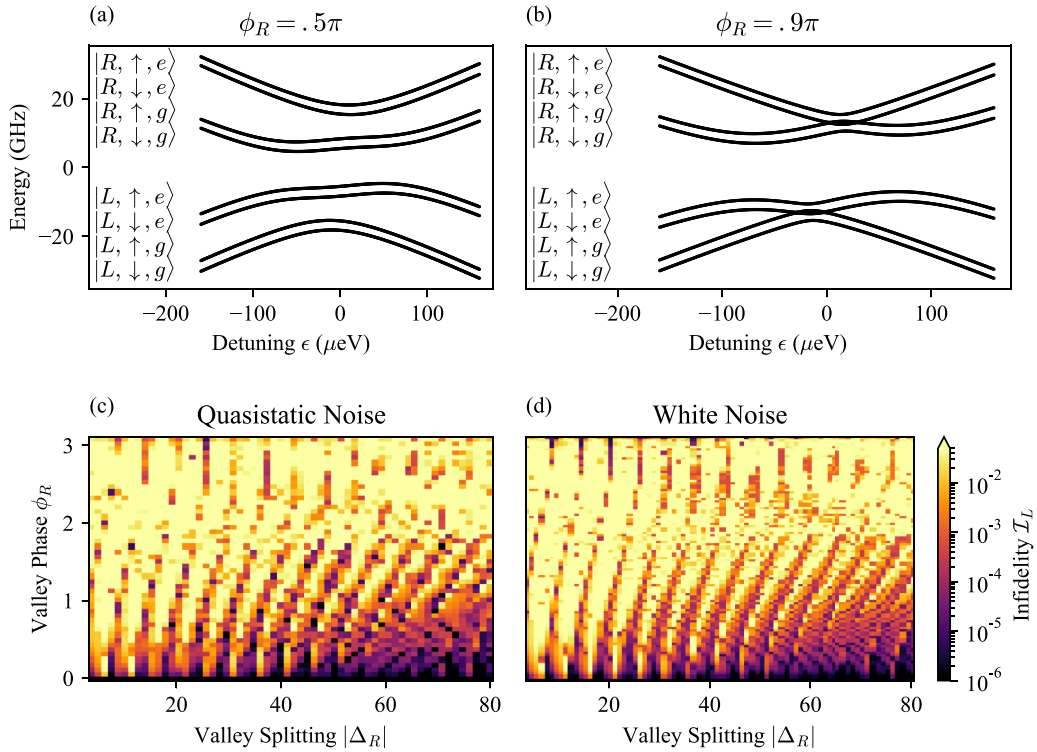

FIG. 6. Simulation of the valley model. (a), (b) Show the energy spectra of a DQD with the additional valley DOF. The spectra are plotted for $t_c = 40\,\mu\text{eV}$, $E_z/(g\mu_B) = 100\,\text{mT}$ (chosen for clarity), $\Delta B_x = 20\,\text{mT}$, $\Delta B_z = 10\,\text{mT}$, $|\Delta_R| = 40\,\mu\text{eV}$. (a) Calculated for a valley phase of $\phi_R = 0.5\pi$ and (b) for a valley phase of $\phi_R = 0.9\pi$, where additional avoided crossings appear. (c), (d) Show Monte Carlo simulations of a flopping-mode qubit driven by a smoothed rectangular pulse including the valley DOF. The simulation was performed with magnetic fields of $\Delta E_z/(g\mu_B) = 20\,\text{mT}$, $\Delta B_x = 2\,\text{mT}$, $\Delta B_z = 0.4\,\text{mT}$ and the parameters $t_c = 100\,\mu\text{eV}$, $A \approx 422\,\mu\text{eV}$, $R_{\text{tanh}} \approx 8.1$, and $\Delta_L = 60\,\mu\text{eV}$. (c) Shows a Monte Carlo simulation of quasistatic noise with a standard deviation of $\sigma_\epsilon = 15\,\mu\text{eV}$. The infidelity shows strong oscillations in the valley phase. If the pulse can be tuned away from a maximum of the oscillation, then the valley splitting should allow high-fidelity gates. (d) Shows a Monte Carlo simulation of white noise with a spectral noise density of $\sqrt{S} = 0.07\,\text{neV}/\sqrt{\text{Hz}}$. The infidelity shows the same oscillations in the valley phase as in (c).

valley excitations as leakage. The resulting energy spectrum is plotted in Figs. 6(a) and 6(b). One can see that the valley-orbit interaction can create new (avoided) crossings depending strongly on the valley phase difference $\Delta\phi = \arg(\Delta_L^* \Delta_R)$ [here $\Delta\phi = \arg(\Delta_R)$] between the two QDs. These new crossings pose additional adiabaticity restrictions on the pulse to avoid valley excitations.

For the simulation of the valley-splitting model, we perform a pulse optimization and noise simulations similar to the preceding section. In the gradient-based optimization, the optimized pulses from the model without valley states serve as initial values in the optimization of the valley model. We use the fidelity measure from Eq. (4) because it only relies on the truncated propagator on the computational space. In Figs. 6(c) and 6(d), we investigate the performance of a parameter combination that yielded excellent fidelities in the absence of valley splittings. The dependence on the valley-splitting magnitude $|\Delta_R|$ and phase ϕ_R in the right QD shows that the fidelity drops to unacceptable values for most of the valley-splitting configurations. Our strong-driving method only works for a very small phase difference, when the pulse is also adiabatic with respect to the valley DOF. This requirement is unlikely to be fulfilled reliably in practice. A simulation without noise can be found in Figs. 11(c) and 11(d).

In the strong-driving mode, we are certain to pass all (avoided) crossings in the energy spectrum, but we want to discuss the prospect of avoiding crossings in the weak-driving mode by appropriate choice of the working point. A simulation of the valley model in the weak-driving regime with the cosine pulse shape as shown in Fig. 3(a) is plotted in Fig. 7. The simulated parameter set was extracted from an experimental realization of the flopping-mode qubit [20]. The result shows a strong dependence on the valley-splitting configuration with local extrema. The simulation results agree with the experimental results in [20] if we assume a favorable valley-splitting configuration.

The features in the infidelity in Fig. 7 can be explained with the corresponding energy spectrum of the valley model. The infidelity contributions at zero valley phase difference $\phi_R = 0$ and $|\Delta_R| \approx 18\,\mu\text{eV}$ or $|\Delta_R| \approx 80\,\mu\text{eV}$ are linked to harmonic excitations, where the excitation energy of the driven transition equals the splitting of other transitions (see Appendix C for details). The blue dashed-dotted line marks valley configurations where the first two excited states are degenerate in energy, and we need to redefine the computational space above this line to drive spinlike transitions. Each feature that increases the infidelity does not only depend on the sample-depending valley splitting but also on variable parameters like the pulse parameters or magnetic field values. The presence

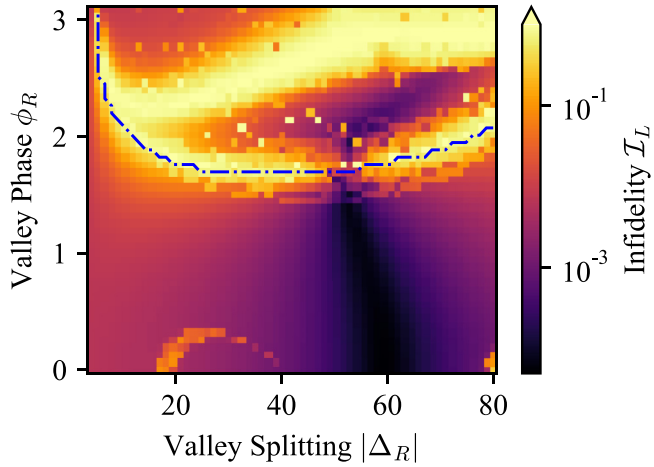

FIG. 7. Influence of the valley splitting in the weak-driving regime. The simulation was performed with experimentally realized parameters [20] with a magnetic field with $E_z/(g\mu_B) = 209\,\mathrm{mT}$, $\Delta B_x = 15\,\mathrm{mT}$, and $\Delta B_z = 0.27\,\mathrm{mT}$, and a tunnel coupling of $t_c = 23\,\mu\mathrm{eV}$. We assumed $\Delta_L = 60\,\mu\mathrm{eV}$ just like in the simulation for Fig. 6 and simulated a pulse of cosine shape as in Fig. 3(a) with an amplitude of $A = 0.42\,\mu\mathrm{eV}$ and an offset $\epsilon_0 = 5.4\,\mu\mathrm{eV}$. Additionally, we simulated quasistatic electric noise with a standard deviation of $\sigma_\epsilon = 0.5\,\mu\mathrm{eV}$. Along the blue dashed-dotted line, the first two excited states are degenerate. Below the line, we drive transitions to the first excited state and above the line to the second excited state.

of the valley DOF thus necessitates an individual optimization of the pulse.

In conclusion, the presence of the valley DOF complicates the driving of the flopping-mode qubit. The expected performance relies on a favorable valley-splitting configuration, and recent studies indicate that the valley splitting in the two dots of a DQD are random and uncorrelated [32]. When flopping-mode qubits are fabricated in large numbers in a silicon-based quantum processor, we predict that a relevant fraction will not outperform conventional EDSR driving due to an unfavorable valley splitting configuration. This fraction could be reduced if the processor can vary the physical positions of the DQDs used for flopping-mode qubits and is calibrated for the valley splitting. Also, a fraction of unusable flopping-mode qubit locations could be mitigated by the implementation of redundant flopping-mode qubit locations. Another prospect is the research in fabrication and tuning methods to control the valley splitting [32,44–46].

V. SUMMARY AND OUTLOOK

We investigated the performance of the flopping-mode qubit with quantum dynamic simulations and pulse optimizations using the optimal control package QOPT [34] and publish the source code on the QOPT applications repository [33] simultaneously to the paper. We demonstrated that driving the flopping-mode qubit with a large pulse amplitude decreases the noise susceptibility and achieves high Rabi frequencies at low magnetic field gradients with the strong displacement of an electron in a DQD. The simulations indicate excellent fidelities even in presence of strong noise sources. In direct comparison to conventional EDSR, the fidelity can be improved by more than two orders of magnitude.

The noise robustness can be attributed to the lower magnetic field gradients and the discreteness of the possible dot positions in-between interdot transitions in the DQD and this discreteness can be fully leveraged by an appropriate choice of the pulse. We developed a smoothed rectangular pulse form to optimize the manipulation in the strong-driving regime. To evaluate the suitability of this pulse form and guide the choice of parameters, we discussed the features of the pulse discreteness and the duty cycle tuning on the qubit performance. Our simulations indicate that the rectangular pulse can further increase the noise insensitivity and the Rabi frequency. In addition, the rectangular pulse can reduce the power dissipation and requirements on the pulse generation.

Leakage caused by orbital excitation due to LZ transitions proved to be one limitation of the rectangular pulse scheme in the strong-driving regime. To avoid diabatic transitions, a small Zeeman splitting E_Z and a strong tunnel coupling t_c are required, while the pulse steepness $R_{\tanh}$ shows a tradeoff between more adiabatic transitions and an increased noise sensitivity. The flopping-mode qubit makes effective use of the small magnetic field gradient and reaches Rabi frequencies of more than $\omega_R/2\pi = 60\,\mathrm{MHz}$ for realistic magnetic field gradients.

Extending the model by a valley DOF, which is present in silicon-based devices, can seriously deteriorate the qubit performance in case of an unfavorable valley-splitting configuration. This valley splitting is a material parameter and difficult to predict or manipulate after the fabrication. A pulse optimization including amplitude and offset depending on a given valley splitting is required. Furthermore, the possible drive amplitude is strongly limited.

While the concept has in principle clear advantage, the implementation in Si/SiGe appears to be hindered by the presence of low-lying excited valley states. An ability to achieve a consistently large valley splitting, such as typically found in MOS devices, or identical valley coupling phases, could likely significantly improve the prospects. For other material systems such as GaAs/AlGaAs or Ge/SiGe, low-lying valley states can be avoided, but different dephasing parameters due to the hyperfine interaction and SO coupling, respectively, would have to be considered.

Another interesting idea for a future study would be the application of similar pulse forms to a resonant SWAP gate. This is a two-qubit gate, where two electrons are placed in a DQD and the exchange interaction is pulsed in resonance with the longitudinal magnetic field gradient ΔB_z across the DQD [47].

A further improvement of the simulation could be the inclusion of orbital and valley relaxation as T_1 process, by solving a Lindblad master equation of the form

$$\dot{\rho} = -\frac{i}{\hbar}[H_V, \rho] + \sum_{i\in\{O,V\}} \gamma_i \left(L_i \rho L_i^\dagger - \frac{1}{2}\{L_i^\dagger L_i, \rho\} \right), \quad (13)$$

where ρ is the systems density matrix, H_V the valley Hamiltonian defined in Eq. (12), γ_i are the relaxation rates, and L_i the relaxation operators on the orbital or valley space. The orbital

relaxation rate depends mainly on the detuning $\gamma_O(\epsilon(t))$ and the valley relaxation rate additionally on the valley splittings $\gamma_V(\epsilon, \Delta_L, \Delta_R)$. The correct treatment of the relaxation processes could reduce the population of leakage states and thus increase the fidelity and make the simulation more accurate in settings where leakage cannot be avoided. Another noise source to be included is the stability of the micromagnets at the low total magnetic fields [19].

As the research on the valley splitting progresses and new insights on the distribution of valley splittings are obtained, it would become interesting to simulate the expected infidelity distribution for a given valley-splitting distribution. This distribution can then be optimized with an included valley-dependent optimization of the pulse amplitude, offset, and envelope or the application of more advanced quantum optimal control methods, for example, to avoid leakage [48].

ACKNOWLEDGMENTS

We thank L. Geck for helpful discussions on the feasibility of creating smoothed rectangular pulses with cryoelectronics. We thank L. Schreiber and M. Oberländer for proofreading the manuscript. This work has been funded by the Federal Ministry of Education and Research (Germany), funding code Grant No. 13N15652 (QUASAR). We acknowledge support from the Impulse and Networking Fund of the Helmholtz Association.

F. Butt performed preliminary studies under the supervision of J. Teske, P. Cerfontaine, and H. Bluhm. J. Teske designed the pulse schemes, developed the optimization algorithm, programmed the simulations in this manuscript, analyzed the data, and wrote the manuscript with guidance by G. Burkard and H. Bluhm.

H. Bluhm is coinventor of patent applications that cover the flopping-mode EDSR as driving mode.

APPENDIX A: PULSE OPTIMIZATION

In this Appendix, we present the construction details of the rectangular pulse scheme using analytic and numeric pulse optimization. We start with a discussion of the degrees of freedom of the control pulses and the target operation. Then we describe the time domain optimization with the QOPT package and how the time discretization is chosen. Finally, we explain the actual optimization algorithm for the cosine pulse and the more complicated case of the rectangular pulse, which requires an accurate estimation of the achievable Rabi frequency and the effective resonance frequency for the optimization of the discrete pulse time.

The relevant degrees of freedom for a quantum gate can be visualized using the group isometry of SU(2) and SO(3), whereby any target evolution of a qubit can be described as rotation on the Bloch sphere. If the driving is resonant, then the rotation axis lies in the xy plane so that it can be described by the azimuth angle θ of the rotation. This azimuth angle θ and the rotation angle ϕ are the two relevant degrees of freedom that describe a resonantly driven quantum gate.

The azimuth angle θ can be tuned using a phase shift of the control pulses. This tuning step is straightforward because any phase shift in the control pulse directly corresponds to a shift in θ. To reduce the number of optimization parameters and the number of cost functions of the optimization, we start with an optimization of the rotation angle ϕ. This is effectively achieved by choosing a state infidelity as the cost function. Thereby, we assume our qubit to be initially in the ground state and drive a full π rotation to the first-excited state. Since we assume the orbital splitting to be larger than the Zeeman splitting, this is a spinlike transition.

We perform the simulation and optimization with the optimal control package QOPT making use of the support of analytic gradients. For this purpose we only need to implement our pulse parametrization and derivatives of this parametrization.

Our pulses possess four degrees of freedom, being the amplitude, frequency, length, and phase shift, but in the strong-driving regime not all parameters can be used effectively because the dynamics are insensitive to changes of the amplitude. Further, the pulse frequency must be chosen resonant to the spin precession frequency and this choice must be consistent with the pulse because the effective average Zeeman splitting depends on the electron position $\Delta B_z \neq 0$. The phase shift is used to control the azimuth angle θ of the quantum gate. The pulse length as remaining DOF can be optimized to control the rotation angle ϕ.

The optimal control package QOPT operates with fixed time steps but we can use a scalar time-stretching parameter s_t to introduce an effective optimization of the pulse length. This time-stretching parameter is absorbed into the Hamiltonian using the identity

$$U = e^{-i\hbar(ts_t)H} = e^{-i\hbar t(s_t H)}. \tag{A1}$$

1. Time discretization

A crucial step in the optimization is the choice of the time discretization into time steps of length δt because a too long δt can limit the accuracy, while a too short δt decreases the numerical efficiency. We thus need to identify the longest δt that resolves all relevant dynamics of our system. Only the orbital dynamics are relevant for the choice of δt because they are much faster than the spin dynamics. Let us consider the orbital Hamiltonian

$$H_O(\epsilon(t)) = \frac{\epsilon(t)}{2}\tau_z + t_c\tau_x \tag{A2}$$

and two unitary propagators U_1, U_2 with different time discretizations

$$U_1 = \prod_{k=1}^{2} e^{H(\epsilon(k\delta t))\delta t},$$

$$U_2 = e^{H(\epsilon(0))2\delta t},$$

such that U_1 is sampled in two time steps of δt and U_2 is sampled with one time step $2\delta t$. Next, we estimate how small δt needs to be chosen that the discretization in steps of δt and $2\delta t$ yields approximately the same result. Therefore, we calculate the deviation ΔU of these two propagators with the Baker-Campbell-Hausdorff formula to be

$$\Delta U = U_1 U_2^\dagger \approx \exp\{(H(\epsilon(0)) - H(\epsilon(\delta t)))\delta t \tag{A3}$$

$$- 2\delta t^2[H(\epsilon(0)), H(\epsilon(\delta t))]\}. \tag{A4}$$

We can now identify criteria that ensure ΔU to be close to unity. From (A3) we identify the first condition to be

$$\delta\epsilon\delta t \ll 1 \tag{A5}$$

with $\delta\epsilon = [\epsilon(0) - \epsilon(\delta t)]/2$, and calculating the commutator in (A4) gives the second condition

$$4t_c\delta t^2\delta\epsilon \ll 1. \tag{A6}$$

Using the maximum values of the pulse derivatives by time as bound for $\delta\epsilon \approx \delta t \frac{\partial\epsilon}{\partial t}$, we can reformulate the conditions for both pulses in terms of the number of time steps n_t and the total pulse time T:

	Cosine	Rectangular
C 1	$n_t \gg \sqrt{T^2 E_z A}$	$n_t \gg \sqrt{T^2 A R_{\tanh}\frac{E_z}{\pi}}$
C 2	$n_t \gg (T^3 4t_c E_z A)^{1/3}$	$n_t \gg (T^3 4t_c A R_{\tanh}\frac{E_z}{\pi})^{1/3}$

2. Cosine pulse optimization

For the cosine pulse, we optimize the time-stretching parameter s_t and the pulse frequency ω. We use s_t to match the gate time with the Rabi frequency and optimize ω to match the resonance frequency of the qubit. The amplitude and phase remain constant during the optimization.

We calculate initial values for the optimization from the Rabi driving theory [49]. First, we transform the time-dependent Hamiltonian $H(\epsilon(t))$ into the eigenbasis of the Hamiltonian at the central position $H(\epsilon_0)$ with the basis transformation $V(\epsilon_0)$. The eigenvalues of

$$V(\epsilon_0)H(\epsilon_0)V(\epsilon_0)^\dagger = \mathrm{diag}(E_1, E_2, E_3, E_4) \tag{A7}$$

are sorted in ascending order $E_1 \leqslant E_2 \leqslant E_3 \leqslant E_4$. We want to drive the spinlike transition of resonance frequency $\omega_{\mathrm{res}} = E_2 - E_1$, while the electron remains in the orbital ground state. The Rabi frequency ω_R can be approximated by the off-diagonal element corresponding to the transition [50]

$$\omega_R \approx A\left(\frac{\partial H(\epsilon)}{\partial\epsilon}\bigg|_{\epsilon_0}\right)_{[0,1]} \approx [H(A) - H(-A)]_{[0,1]}. \tag{A8}$$

3. Rectangular pulse optimization

Tuning the smoothed rectangular pulse is more complicated since we require the pulse to consist of a number N_P of full resonance periods. In addition, we want to avoid a mixed discrete and continuous optimization for the sake of simplicity, so we require N_P to be constant during the continuous optimization. In consequence, the pulse length and frequency cannot be varied independently. We calculate the optimal number of driving periods before the optimization and optimize only the time-stretching parameter s_t and the duty cycle parameter c_{dc} with a gradient-based optimization algorithm.

The duty cycle tuning can be used to effectively decrease the driving strength and thereby change the Rabi frequency ω_R. ω_R is maximal when $c_{\mathrm{dc}} = 0$ and drops to zero for $c_{\mathrm{dc}} = 1$. We want to choose c_{dc} as small as possible because large c_{dc} values lead to longer pulses and an increased noise susceptibility. Therefore, the optimal N_p is the smallest number of driving periods that are sufficient to realize the target gate.

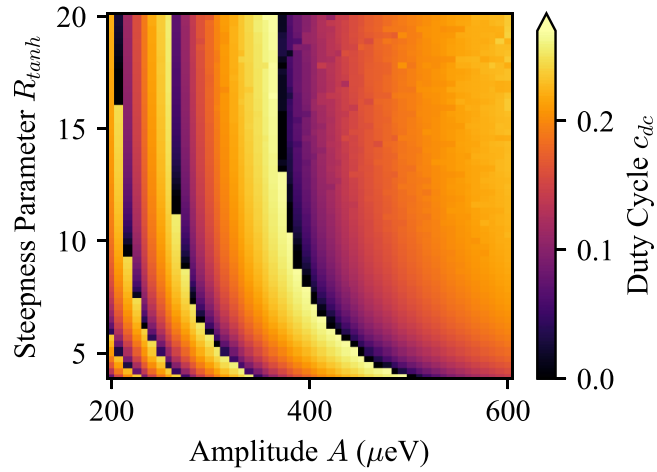

FIG. 8. Duty cycle c_{dc} from the pulse optimization belonging to Figs. 4(c) and 4(d). The discontinuities in c_{dc} correspond to the changes in pulse length and thus changes in the Rabi frequency ω_R marked by green dashed lines in Figs. 4(c) and 4(d).

To give an example for the tuning range of the duty cycle, Fig. 8 shows the optimized c_{dc} values from the pulse optimization leading to the fidelities plotted in Figs. 4(c) and 4(d). It can be observed that the optimal c_{dc} rises monotonically with the amplitude A and the steepness parameter $R_{\tanh}$ to compensate the increased driving efficiency until N_P can be reduced by one and the optimal c_{dc} value is reset to 0. The required range of c_{dc} values is related to the number of resonance periods N_P. The lower N_P is, the stronger one needs to tune c_{dc} to adjust the total pulse time to the next integer multiple of the resonance time.

a. Rabi frequency estimation

We calculate an estimation of the maximal ω_R at $c_{\mathrm{dc}} = 0$ by solving the effective spin Hamiltonian

$$H_S = E_z\frac{\sigma_z}{2} + \Delta B_x\langle\tau_z\rangle\frac{\sigma_x}{2}, \tag{A9}$$

where $\langle\tau_z\rangle = \langle 0|\tau_z|0\rangle$ is the expectation value of the τ_z operator in the instantaneous ground state. This expectation value can be calculated from the orbital Hamiltonian

$$H_O = \epsilon\frac{\tau_z}{2} + 2t_c\frac{\tau_x}{2} \tag{A10}$$

and has the analytical solution

$$\langle\tau_z\rangle = \frac{\epsilon\left(\epsilon - \sqrt{\epsilon^2 + 4t_c^2}\right)}{\epsilon^2 - \epsilon\sqrt{\epsilon^2 + 4t_c^2} + 4t_c^2}. \tag{A11}$$

Finally, we calculate the Rabi frequency ω_R in the rotating reference frame as the average over one period of the driving pulse:

$$\omega_R = \Delta B_x\frac{\sigma_x}{T_{\mathrm{res}}}\int_0^{T_{\mathrm{res}}}\langle\tau_z(\epsilon(t))\rangle dt. \tag{A12}$$

The discreteness of the pulse leads to systematic errors even after the optimization. These errors lead only to small

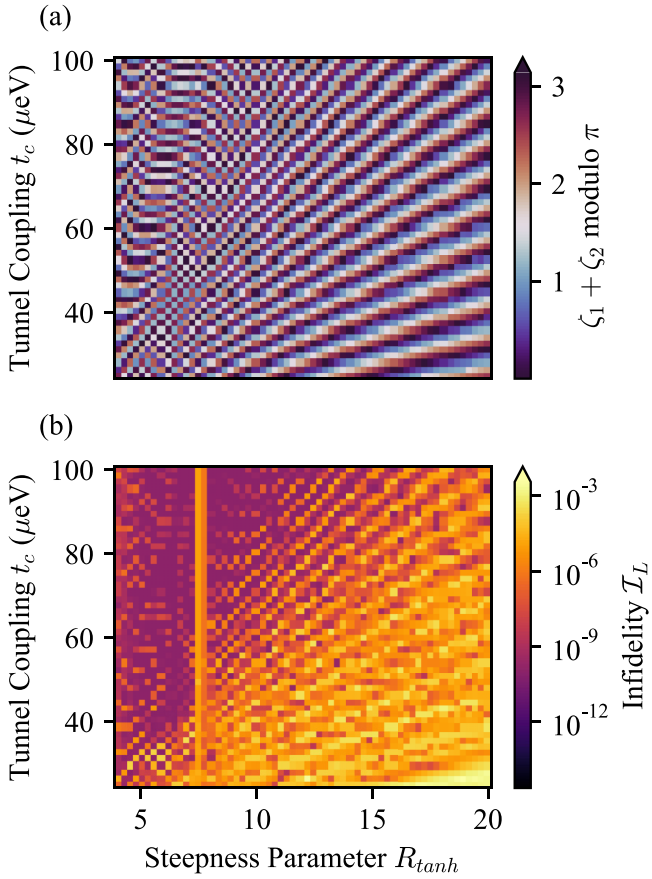

FIG. 9. Landau-Zener-Stückelberg oscillation pattern. (a) Shows the sum of the accumulated phases $\zeta_1 + \zeta_2$ between transition through the avoided crossing modulo 2π for the simulation in Figs. 5(a) and 5(b) in the main text. The pattern can also be found in the infidelity calculated in the absence of noise plotted in (b).

infidelities but are visible for example as a vertical line in Figs. 5(a) and 5(b) around $R_{\text{tanh}} = 8$. At this line, N_P changed by one.

Furthermore, precise initial values are required for the optimization because the LZS oscillations (see Appendix B) create such a rough optimization landscape that a pure gradient-based optimization quickly converges to the nearest local optimum. We therefore start by simulating a grid of parameter combinations around the presumed location of the global optimum. The parameter combination with the lowest infidelity is then chosen as the initial set of values.

b. Effective Zeeman splitting

We further improve the convergence of the optimization by introduction of orthogonal control parameters. c_{dc} and s_t are not orthogonal, in the sense that any change in c_{dc} alters the average occupation of the QDs and changes the effective resonance frequency ω_{res} because of the longitudinal magnetic field gradient ΔB_z in the Hamiltonian in (1). We now calculate the shift in ω_{res} and the corresponding compensation in s_t analytically and include it in the pulse parametrization.

For any duty cycle parameter c_{dc}, we spend $c_{\text{dc}}/2T_{\text{res}}$ longer in the right QD. For this time, the resonance frequency is shifted by ΔB_z. Thus, the new effective resonance frequency

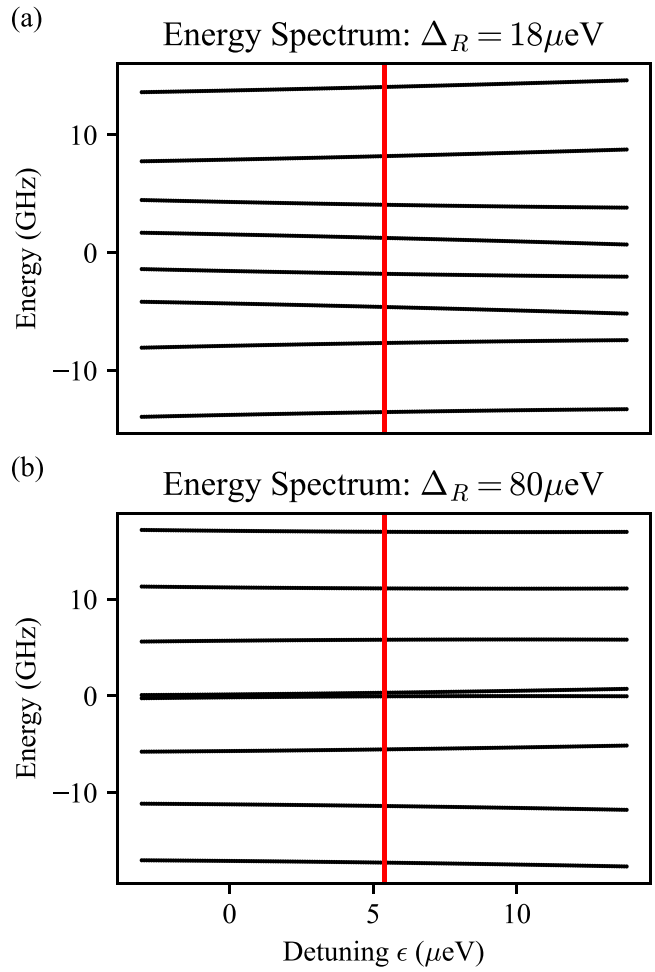

FIG. 10. Selected energy spectra with parameters of the weak-driving mode with valley DOF as plotted in Fig. 7. In both plots we discuss energy spectra for purely real valley splittings in both dots, i.e., $\Delta\phi = 0$. The red lines mark the operation point in the pulse offset ϵ_0 and the plotted range corresponds to $10A$. The energy spectra can explain leakage into certain states. In (a) the energy difference between the ground and first-excited states equals approximately the energy splitting between the first- and the third-excited states. In (b) the energy difference between the ground the the first-excited states equal approximately the energy difference between the first- and the second-excited states.

is $\omega'_{\text{res}} = E_z(1 + \frac{c_{\text{dc}}\Delta B_z}{2E_z})$, and we need to multiply s_t by an additional correction of $s_C = 1/(1 + \frac{c_{\text{dc}}\Delta B_z}{2E_z}) \approx 1 - \frac{c_{\text{dc}}\Delta B_z}{2E_z}$.

APPENDIX B: LANDAU-ZENER-STÜCKELBERG INTERFERENCE

In Figs. 5(a) and 5(b) in the main text, we can weakly see an oscillation pattern in the infidelity. This pattern can be explained by Landau-Zener-Stückelberg (LZS) interferometry [40]. The LZS theory describes coherent excitations that occur as result of periodic passages of an avoided crossing. Driving the detuning induces such passages in the orbital DOF in the flopping-mode qubit, where the avoided crossing is at the minimum of the orbital splitting at $\epsilon = 0$ and excitations correspond to leakage into the excited orbital state. The reso-

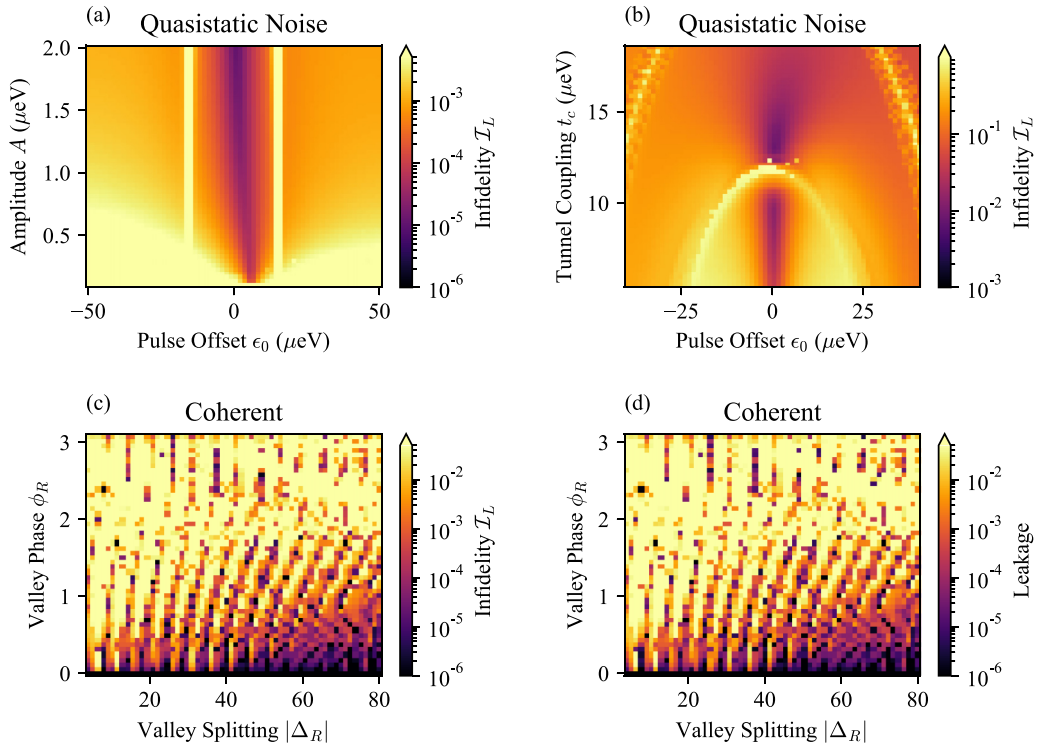

FIG. 11. (a) Reproduction of the infidelity in Fig. 4(b) in [20] measured by Croot *et al.* The simulation was performed with the parameters measured in [20]. We therefore used magnetic field gradients of $\Delta B_x = 15\,\mathrm{mT}$ and $\Delta B_z = 0.27\,\mathrm{mT}$, a total magnetic field of $B_z = 209.4\,\mathrm{mT}$, a tunnel coupling of $2t_c = 23\,\mu\mathrm{eV}$, and quasistatic noise with a standard deviation of $\sigma_\epsilon = 0.5\,\mu\mathrm{eV}$. (b) Reproduction of the infidelity in Fig. 4(b) in [21] simulated by Benito *et al.* A second-order charge noise sweet spot at about $t_c = 13\,\mu\mathrm{eV}$ can be seen, but the minimum is shifted towards the center $\epsilon = 0$. The simulation was performed with the parameters employed in [20]. We therefore used magnetic field gradients $\Delta B_x = 17.3\,\mathrm{mT}$ and $\Delta B_z = 4.32\,\mathrm{mT}$ at a total magnetic field of $B_z = 207\,\mathrm{mT}$, driving with an amplitude of $A = 2.1\,\mu\mathrm{eV}$ and simulating quasistatic noise of standard deviation $\sigma_\epsilon/\hbar = 2.5\,\mu\mathrm{eV}$. (c), (d) Show the coherent simulation of the flopping-mode qubit including the valley splitting but without noise. The simulation was performed with the same parameters as in Fig. 6. The infidelity (c) and the leakage (d) look almost identical, indicating that leakage is the dominant contribution to the infidelity.

nance condition for LZS interferometry is linked to the phases ζ_1 and ζ_2 accumulated between the passages of the avoided crossing. In the slow-passage limit, the resonance condition can be reduced to

$$\zeta_1 + \zeta_2 + 2\phi_S = k\pi, k \in \mathbb{N}, \tag{B1}$$

where ϕ_S is the Stückelberg phase. The correspondence between the resonance pattern in the infidelity in Figs. 5(a) or 9(b) and the sum of the accumulated phases in Fig. 9(a) indicates that LZS oscillations pose the main contribution of infidelity in the absence of noise in this simulation.

APPENDIX C: HARMONIC EXCITATION

This Appendix discusses the energy spectrum of valley-splitting model to explain features in Fig. 7. For the plots in Fig. 10, we select two points of interest from the simulation with a purely real valley parameter $\Delta_R = 18\,\mu\mathrm{eV}$ in (a) and $\Delta_R = 80\,\mu\mathrm{eV}$ in (b). At these points we observe a local increase in the infidelity in Fig. 7 that cannot be explained with diabatic valley excitation because the valley phase difference is zero.

We explain these features in the infidelity by harmonic excitation, in the sense that multiple transitions have an energy splitting identical to the driven transition. The Hamiltonian $H_V(\epsilon_0)$ from Eq. (12) has the eigenvalues $e_1, \ldots, e_8$ in ascending order and eigenvectors $v_1, \ldots, v_8$, where v_1 and v_2 span the computational space. Thus, our pulse is driven with the frequency $e_2 - e_1 = \omega \approx E_z$. Now we observe an increase in the leakage into state v_4 for $\Delta_R = 18\,\mu\mathrm{eV}$ in our simulation. The reason for this increase in leakage is that $e_2 - e_1 = \omega \approx e_4 - e_2$ as can be seen in Fig. 10(a). Similarly, we observe leakage into v_3 around $\Delta_R = 80\,\mu\mathrm{eV}$ and Fig. 10(b) shows that here $\omega \approx e_3 - e_2$ holds. We conclude that the observed leakage increases at these points because our pulse drives multiple transitions resonantly with the same energy difference.

APPENDIX D: REPRODUCTION CROOT *ET AL.*

Croot *et al.* demonstrated the feasibility of flopping-mode driving experimentally [20]. They leveraged the large electric dipole moment to increase the driving efficiency by nearly three orders of magnitude in the zero detuning configuration. This enabled them to reach Rabi frequencies of up to 8 MHz with about 250 times less microwave power compared to standard EDSR.

We qualitatively reproduce Fig. 4(b) from [20] by sweeping the static offset ϵ_0 and the driving amplitude A. Our results are plotted in Fig. 11(a) and the simulation reproduces the

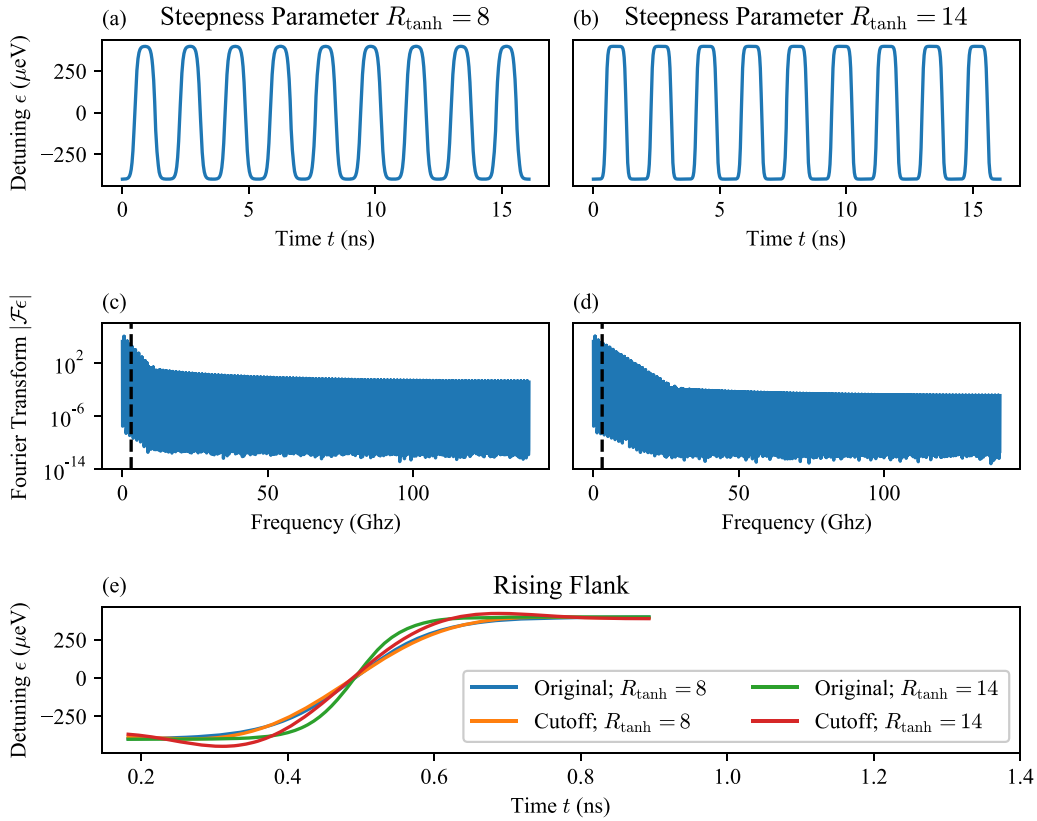

FIG. 12. Spectral analysis of example smoothed rectangular pulses. In (a) and (b) the smoothed rectangular pulses with steepness parameters $R_{\text{tanh}} = 8$ and 14 are plotted. The other pulse parameters are calculated for $E_z/(g\mu_B) = 20\,\text{mT}$, $\Delta B_x = 2\,\text{mT}$, $\Delta B_z = 0.4\,\text{mT}$, $t_c = 100\,\mu\text{eV}$, and $A = 400\,\mu\text{eV}$, as they appear for example in Fig. 4. It can be observed that the larger R_{tanh} leads to sharper transitions in the pulse. The absolute values of the corresponding Fourier transforms are plotted in (c) and (d), where the black dashed line marks a cutoff frequency of $f_c = 3\,\text{GHz}$. In (e) the rising flank of both pulses is plotted with the same pulses when generated with a cutoff frequency f_c. Due to the symmetry and periodicity, the plot contains the full pulse information. For simplicity, we use a symmetric filter not respecting causality for this illustration. It can be seen that a bandwidth of 0 to f_c is sufficient to generate the smoother pulse with $R_{\text{tanh}} = 8$ but is insufficient for the sharper pulse with $R_{\text{tanh}} = 14$.

fidelity maximum near zero detuning offset $\epsilon_0 = 0$ with a slight shift to positive detuning offsets. Croot *et al.* do not find the local infidelity maximum at the spin-orbit degeneracy point, possibly because they sample the offset ϵ_0 too coarsely or because other dephasing channels dominate. We cannot reproduce their high Rabi frequencies for large detuning offsets $|\epsilon| > 30\,\mu\text{eV}$, likely because the electron is strongly confined for these values such that the driving relies on shifts of the QD, which are not included in our model.

APPENDIX E: REPRODUCTION BENITO *ET AL.*

Benito *et al.* investigated the susceptibility of the flopping-mode qubit to electric noise with analytical calculations. They predicted a second-order sweet spot for the qubit, where it would be insensitive to quasistatic detuning shifts up to second order. We can reproduce a local minimum in the infidelity but it is shifted more towards the symmetric position $\epsilon = 0$. The differences between Figs. 11(b) and 4(b) in [21] can be explained by the fact that the numerical simulations capture the influence of leakage explicitly than the analytical calculations employed in [21].

The main difference between the driving mode investigated in [20,21] and the driving mode presented in this paper are the relations of magnetic field strengths, tunnel coupling, and driving amplitude. They operate at a much larger spin-orbit mixing and achieve a better relation of Rabi frequency to driving power at the cost of an increased noise susceptibility.

APPENDIX F: PULSE BANDWIDTH

In this Appendix, we present an example analysis of the bandwidth required to generate the discussed smoothed rectangular pulses. In Fig. 12, we show two pulses of different steepness for typical parameters used in the simulations. The plots of the pulses in Figs. 12(a) and 12(b) show again the influence of the steepness parameter R_{tanh} and the corresponding Fourier transform in Figs. 12(d) and 12(e) show that the sharper pulse has a larger spectral weight at higher frequencies, as expected.

To investigate the influence of a limited bandwidth, we apply a cutoff at $f_c = 3\,\text{GHz}$ and apply the inverse Fourier transformation. The rising flank of the resulting pulse is plotted in Fig. 12(e), where it can be observed that the pulse with $R_{\text{tanh}} = 8$ is not significantly deformed, while the the pulse with $R_{\text{tanh}} = 14$ is smoothed by the application of the cutoff frequency. Note that the simulation results

indicate that the accuracy of the transition is much more important that the exact shape at the plateaus, where the pulse values saturate $\epsilon \approx A$. We conclude that the proposed pulses with appropriate pulse steepness can be generated by commercially available arbitrary waveform generators. Following this procedure, the required bandwidth can be found for any parameter set. The two critical parameters are the pulse steepness R_{tanh} and the resonance frequency determined by E_z.

[1] A. Noiri, K. Takeda, T. Nakajima, T. Kobayashi, A. Sammak, G. Scappucci, and S. Tarucha, Fast universal quantum gate above the fault-tolerance threshold in silicon, Nature (London) **601**, 338 (2022).

[2] X. Xue, M. Russ, N. Samkharadze, B. Undseth, A. Sammak, G. Scappucci, and L. M. K. Vandersypen, Quantum logic with spin qubits crossing the surface code threshold, Nature (London) **601**, 343 (2022).

[3] S. G. J. Philips, M. T. Madzik, S. V. Amitonov, S. L. de Snoo, M. Russ, N. Kalhor, C. Volk, W. I. L. Lawrie, D. Brousse, L. Tryputen, B. P. Wuetz, A. Sammak, M. Veldhorst, G. Scappucci, and L. M. K. Vandersypen, Universal control of a six-qubit quantum processor in silicon, Nature **609**, 919 (2022).

[4] A. R. Mills, C. R. Guinn, M. J. Gullans, A. J. Sigillito, M. M. Feldman, E. Nielsen, and J. R. Petta, Two-qubit silicon quantum processor with operation fidelity exceeding 99%, Sci. Adv. **8**, eabn5130 (2022).

[5] G. Burkard, T. D. Ladd, J. M. Nichol, A. Pan, and J. R. Petta, Semiconductor spin qubits, arXiv:2112.08863.

[6] V. Langrock, J. A. Krzywda, N. Focke, I. Seidler, L. R. Schreiber, and L. CywiÅski, Blueprint of a scalable spin qubit shuttle device for coherent mid-range qubit transfer in disordered Si/SiGe/SiO_2, arXiv:2202.11793.

[7] J. M. Boter, J. P. Dehollain, J. P. G. van Dijk, Y. Xu, T. Hensgens, R. Versluis, H. W. L. Naus, J. S. Clarke, M. Veldhorst, F. Sebastiano, and L. M. K. Vandersypen, Spiderweb Array: A Sparse Spin-Qubit Array, Phys. Rev. Appl. **18**, 024053 (2022).

[8] X. Xue, B. Patra, J. P. G. van Dijk, N. Samkharadze, S. Subramanian, A. Corna, B. Paquelet Wuetz, C. Jeon, F. Sheikh, E. Juarez-Hernandez, B. P. Esparza, H. Rampurawala, B. Carlton, S. Ravikumar, C. Nieva, S. Kim, H.-J. Lee, A. Sammak, G. Scappucci, M. Veldhorst *et al.*, Cmos-based cryogenic control of silicon quantum circuits, Nature (London) **593**, 205 (2021).

[9] S. J. Pauka, K. Das, R. Kalra, A. Moini, Y. Yang, M. Trainer, A. Bousquet, C. Cantaloube, N. Dick, G. C. Gardner, M. J. Manfra, and D. J. Reilly, A cryogenic cmos chip for generating control signals for multiple qubits, Nat. Electron. **4**, 64 (2021).

[10] L. Petit, H. G. J. Eenink, M. Russ, W. I. L. Lawrie, N. W. Hendrickx, S. G. J. Philips, J. S. Clarke, L. M. K. Vandersypen, and M. Veldhorst, Universal quantum logic in hot silicon qubits, Nature (London) **580**, 355 (2020).

[11] C. H. Yang, R. C. C. Leon, J. C. C. Hwang, A. Saraiva, T. Tanttu, W. Huang, J. Camirand Lemyre, K. W. Chan, K. Y. Tan, F. E. Hudson, K. M. Itoh, A. Morello, M. Pioro-Ladrière, A. Laucht, and A. S. Dzurak, Operation of a silicon quantum processor unit cell above one kelvin, Nature (London) **580**, 350 (2020).

[12] A. Mills, D. Zajac, M. Gullans, F. Schupp, T. Hazard, and J. Petta, Shuttling a single charge across a one-dimensional array of silicon quantum dots, Nat. Commun. **10**, 1063 (2019).

[13] I. Seidler, T. Struck, R. Xue, N. Focke, S. Trellenkamp, H. Bluhm, and L. R. Schreiber, Conveyor-mode single-electron shuttling in Si/SiGe for a scalable quantum computing architecture, npj Quantum Inf. **8**, 100 (2022).

[14] A. Noiri, K. Takeda, T. Nakajima, T. Kobayashi, A. Sammak, G. Scappucci, and S. Tarucha, A shuttling-based two-qubit logic gate for linking distant silicon quantum processors, Nat. Commun. **13**, 5740 (2022).

[15] K. C. Nowack, F. H. L. Koppens, Y. V. Nazarov, and L. M. K. Vandersypen, Coherent control of a single electron spin with electric fields, Science **318**, 1430 (2007).

[16] M. Pioro-Ladrière, T. Obata, Y. Tokura, Y.-S. Shin, T. Kubo, K. Yoshida, T. Taniyama, and S. Tarucha, Selective manipulation of electron spins with electric fields, Prog. Theor. Phys. Suppl. **176**, 322 (2008).

[17] J. Yoneda, K. Takeda, T. Otsuka, T. Nakajima, M. R. Delbecq, G. Allison, T. Honda, T. Kodera, S. Oda, Y. Hoshi, N. Usami, K. M. Itoh, and S. Tarucha, A quantum-dot spin qubit with coherence limited by charge noise and fidelity higher than 99.9%, Nat. Nanotechnol. **13**, 102 (2018).

[18] T. Struck, A. Hollmann, F. Schauer, O. Fedorets, A. Schmidbauer, K. Sawano, H. Riemann, N. V. Abrosimov, Ł. Cywiński, D. Bougeard, and L. R. Schreiber, Low-frequency spin qubit energy splitting noise in highly purified $_{28}$Si/SiGe, npj Quantum Inf. **6**, 40 (2020).

[19] R. Neumann and L. R. Schreiber, Simulation of micro-magnet stray-field dynamics for spin qubit manipulation, J. Appl. Phys. **117**, 193903 (2015).

[20] X. Croot, X. Mi, S. Putz, M. Benito, F. Borjans, G. Burkard, and J. R. Petta, Flopping-mode electric dipole spin resonance, Phys. Rev. Res. **2**, 012006(R) (2020).

[21] M. Benito, X. Croot, C. Adelsberger, S. Putz, X. Mi, J. R. Petta, and G. Burkard, Electric-field control and noise protection of the flopping-mode spin qubit, Phys. Rev. B **100**, 125430 (2019).

[22] P. Huang and X. Hu, Spin relaxation in a Si quantum dot due to spin-valley mixing, Phys. Rev. B **90**, 235315 (2014).

[23] M. Benito, X. Mi, J. M. Taylor, J. R. Petta, and G. Burkard, Input-output theory for spin-photon coupling in Si double quantum dots, Phys. Rev. B **96**, 235434 (2017).

[24] X. Mi, M. Benito, S. Putz, D. M. Zajac, J. M. Taylor, G. Burkard, and J. R. Petta, A coherent spin–photon interface in silicon, Nature (London) **555**, 599 (2018).

[25] N. Samkharadze, G. Zheng, N. Kalhor, D. Brousse, A. Sammak, U. C. Mendes, A. Blais, G. Scappucci, and L. M. K. Vandersypen, Strong spin-photon coupling in silicon, Science **359**, 1123 (2018).

[26] X. Mi, J. V. Cady, D. M. Zajac, P. W. Deelman, and J. R. Petta, Strong coupling of a single electron in silicon to a microwave photon, Science **355**, 156 (2017).

[27] A. Stockklauser, P. Scarlino, J. V. Koski, S. Gasparinetti, C. K. Andersen, C. Reichl, W. Wegscheider, T. Ihn, K. Ensslin, and A. Wallraff, Strong Coupling Cavity QED with Gate-Defined Double Quantum Dots Enabled by a High Impedance Resonator, Phys. Rev. X **7**, 011030 (2017).

[28] M. Benito, J. R. Petta, and G. Burkard, Optimized cavity-mediated dispersive two-qubit gates between spin qubits, Phys. Rev. B **100**, 081412(R) (2019).

[29] J. Cayao, M. Benito, and G. Burkard, Programmable two-qubit gates in capacitively coupled flopping-mode spin qubits, Phys. Rev. B **101**, 195438 (2020).

[30] P. M. Mutter and G. Burkard, Natural heavy-hole flopping mode qubit in germanium, Phys. Rev. Res. **3**, 013194 (2021).

[31] V. Reiher and Y. Bérubé-Lauzière, Optimal control of the operating regime of a single electron double quantum dot, arXiv:2104.13571.

[32] B. P. Wuetz, M. P. Losert, S. Koelling, L. E. A. Stehouwer, A.-M. J. Zwerver, S. G. J. Philips, M. T. Madzik, X. Xue, G. Zheng, M. Lodari, S. V. Amitonov, N. Samkharadze, A. Sammak, L. M. K. Vandersypen, R. Rahman, S. N. Coppersmith, O. Moutanabbir, M. Friesen, and G. Scappucci, Atomic fluctuations lifting the energy degeneracy in Si/SiGe quantum dots, Nat. Commun. **13**, 7730 (2022).

[33] J. Teske, qopt-applications: Simulations and optimal control implemented with qopt, https://github.com/qutech/qopt-applications.

[34] J. D. Teske, P. Cerfontaine, and H. Bluhm, QOPT: An Experiment-Oriented Software Package for Qubit Simulation and Quantum Optimal Control, Phys. Rev. Appl. **17**, 034036 (2022).

[35] C. J. Wood and J. M. Gambetta, Quantification and characterization of leakage errors, Phys. Rev. A **97**, 032306 (2018).

[36] V. O. Shkolnikov, R. Mauch, and G. Burkard, All-microwave holonomic control of an electron-nuclear two-qubit register in diamond, Phys. Rev. B **101**, 155306 (2020).

[37] O. E. Dial, M. D. Shulman, S. P. Harvey, H. Bluhm, V. Umansky, and A. Yacoby, Charge Noise Spectroscopy Using Coherent Exchange Oscillations in a Singlet-Triplet Qubit, Phys. Rev. Lett. **110**, 146804 (2013).

[38] E. Kawakami, P. Scarlino, D. R. Ward, F. R. Braakman, D. E. Savage, M. G. Lagally, M. Friesen, S. N. Coppersmith, M. A. Eriksson, and L. M. K. Vandersypen, Electrical control of a long-lived spin qubit in a Si/SiGe quantum dot, Nat. Nanotechnol. **9**, 666 (2014).

[39] L. V. C. Assali, H. M. Petrilli, R. B. Capaz, B. Koiller, X. Hu, and S. Das Sarma, Hyperfine interactions in silicon quantum dots, Phys. Rev. B **83**, 165301 (2011).

[40] S. Shevchenko, S. Ashhab, and F. Nori, Landau–Zener–Stückelberg interferometry, Phys. Rep. **492**, 1 (2010).

[41] T. Ando, A. B. Fowler, and F. Stern, Electronic properties of two-dimensional systems, Rev. Mod. Phys. **54**, 437 (1982).

[42] A. L. Saraiva, M. J. Calderón, X. Hu, S. Das Sarma, and B. Koiller, Physical mechanisms of interface-mediated intervalley coupling in Si, Phys. Rev. B **80**, 081305(R) (2009).

[43] L. J. Sham and M. Nakayama, Effective-mass approximation in the presence of an interface, Phys. Rev. B **20**, 734 (1979).

[44] C. H. Yang, A. Rossi, R. Ruskov, N. S. Lai, F. A. Mohiyaddin, S. Lee, C. Tahan, G. Klimeck, A. Morello, and A. S. Dzurak, Spin-valley lifetimes in a silicon quantum dot with tunable valley splitting, Nat. Commun. **4**, 2069 (2013).

[45] T. McJunkin, E. R. MacQuarrie, L. Tom, S. F. Neyens, J. P. Dodson, B. Thorgrimsson, J. Corrigan, H. E. Ercan, D. E. Savage, M. G. Lagally, R. Joynt, S. N. Coppersmith, M. Friesen, and M. A. Eriksson, Valley splittings in Si/SiGe quantum dots with a germanium spike in the silicon well, Phys. Rev. B **104**, 085406 (2021).

[46] T. McJunkin, B. Harpt, Y. Feng, M. Losert, R. Rahman, J. P. Dodson, M. A. Wolfe, D. E. Savage, M. G. Lagally, S. N. Coppersmith, M. Friesen, R. Joynt, and M. A. Eriksson, SiGe quantum wells with oscillating ge concentrations for quantum dot qubits, Nat. Commun. **13**, 7777 (2022).

[47] A. J. Sigillito, M. J. Gullans, L. F. Edge, M. Borselli, and J. R. Petta, Coherent transfer of quantum information in a silicon double quantum dot using resonant swap gates, npj Quantum Inf. **5**, 110 (2019).

[48] D. Guéry-Odelin, A. Ruschhaupt, A. Kiely, E. Torrontegui, S. Martínez-Garaot, and J. G. Muga, Shortcuts to adiabaticity: Concepts, methods, and applications, Rev. Mod. Phys. **91**, 045001 (2019).

[49] I. I. Rabi, Space quantization in a gyrating magnetic field, Phys. Rev. **51**, 652 (1937).

[50] B. Joecker, P. Cerfontaine, F. Haupt, L. R. Schreiber, B. E. Kardynał, and H. Bluhm, Transfer of a quantum state from a photonic qubit to a gate-defined quantum dot, Phys. Rev. B **99**, 205415 (2019).